



Università degli Studi Mediterranea di Reggio Calabria
Archivio Istituzionale dei prodotti della ricerca

Tensile behaviour of an HDPE geogrid under cyclic loading: experimental results and empirical modelling

This is the peer reviewed version of the following article:

Original

Tensile behaviour of an HDPE geogrid under cyclic loading: experimental results and empirical modelling / Cardile, G; Moraci, Nicola; Pisano, M; Marilene, Pisano. - In: GEOSYNTHETICS INTERNATIONAL. - ISSN 1072-6349. - 24:1(2017), pp. 95-112. [10.1680/jgein.16.00019]

Availability:

This version is available at: <https://hdl.handle.net/20.500.12318/2619> since: 2021-02-18T12:22:22Z

Published

DOI: <http://doi.org/10.1680/jgein.16.00019>

The final published version is available online at: <https://www.icevirtuallibrary.com/doi/full/10.1680/jgein.16.00019>

Terms of use:

The terms and conditions for the reuse of this version of the manuscript are specified in the publishing policy. For all terms of use and more information see the publisher's website

Publisher copyright

This item was downloaded from IRIS Università Mediterranea di Reggio Calabria (<https://iris.unirc.it/>) When citing, please refer to the published version.

(Article begins on next page)

1 **TENSILE BEHAVIOUR OF A HDPE GEOGRID UNDER CYCLIC LOADINGS:**

2 **EXPERIMENTAL RESULTS AND EMPIRICAL MODELLING**

3 G. Cardile¹, N. Moraci² and M. Pisano³

4 ¹ Assistant Professor of Geotechnical Engineering, Ph.D. — *Mediterranea* University of Reggio Calabria, Department of
5 Civil Engineering, Energy, Environment and Materials (DICEAM), Italy- Telephone: +39 0965 169 2213; Telefax: +39 0965
6 1692201, e-mail: giuseppe.cardile@unirc.it (corresponding author)

7 ² Full Professor of Geotechnical Engineering, Ph.D. — *Mediterranea* University of Reggio Calabria, Department of Civil
8 Engineering, Energy, Environment and Materials (DICEAM), Italy- Telephone: +39 0965 169 2263; Telefax: +39 0965
9 1692201, e-mail: nicola.moraci@unirc.it

10 ³ Research Assistant in Geotechnical Engineer, Ph.D. — *Mediterranea* University of Reggio Calabria, Department of Civil
11 Engineering, Energy, Environment and Materials (DICEAM), Italy- Telephone: +39 0965 169 2306; Telefax: +39 0965
12 1692201, e-mail: marilene.pisano@unirc.it

13

14 **ABSTRACT**

15 Residual deformations due to sustained and cyclic loading, acting on full-scale reinforced soil-
16 retaining walls, could lead to an unacceptable serviceability limit state. In the present study, the
17 researchers carried out an extensive experimental program comprising several monotonic and
18 multistage tensile tests on a high-density polyethylene (HDPE) uniaxial extruded geogrid.

19 Based on analysis of the test results, a combined empirical model has been developed that can predict
20 the tensile behaviour of a specific HDPE geogrid subject to cyclic tensile loadings. In detail, the paper
21 aims to show and analyse the effect of cyclic tensile loading histories (varying pre-stress tensile load,
22 frequency, amplitude and number of cycles) on those parameters that are characteristic of hysteresis
23 loops (i.e. maximum and residual strains cumulated during each cyclic loading, tensile stiffness and
24 area of the hysteresis loops).

25 The results showed that the average strain rate and the loading time affect the material's tensile
26 response, as well as the combination of pre-stress tensile load and loading amplitude. The authors also
27 investigated the difference between the load-strain relations for the monotonic test and those for the
28 multistage tests, obtaining that the effects of cyclic loading histories do not entail material degradation.

29

30 KEYWORDS: Geosynthetics, Cyclic loading, Geogrid, Tensile Stiffness, Multistage tensile tests,
31 Empirical model, Ratcheting, Damping

32 **1 INTRODUCTION**

33 Extruded, bonded or woven geogrids are polymeric materials widely used in geotechnical engineering
34 applications as reinforcing elements of granular backfills intended to improve the mechanical
35 behaviour of the soil. During the service life of geosynthetic-reinforced soil (GRS) structures, geogrids
36 may be subjected to cyclic or dynamic loads (both long-term cyclic vehicular loads and short-term
37 seismic loads, if these structures are built in seismic zones), in addition to the sustained tensile load
38 acting under service load conditions (due to the structure's self-weight and to the external dead load).

39 Case histories and studies of the behaviour under serviceability conditions of full-scale reinforced soil-
40 retaining walls and bridge abutments (Tatsuoka *et al.* 1995; Ling *et al.* 2001; Bathurst *et al.* 2002;
41 Koseki *et al.* 2003; Lee and Wu 2004; Koseki *et al.* 2006; Kuwano *et al.* 2014) report unacceptably
42 large residual deformations due to tensile creep and cyclic loading acting on these viscous polymeric
43 materials. To model the behaviour of GRS structures and estimate structural deformation under
44 serviceability conditions using numerical methods (e.g., the finite element method) requires
45 knowledge of the constitutive model that should be adopted for reinforcement and soil, along with
46 definition of the interface model. Therefore, it is first of all essential to define the stress-strain-time
47 relationships of the system's constituent parts (Perkins 2000). Defining the reinforcement's mechanical
48 properties (using monotonic, creep and cyclic tensile tests) is one of the main factors of these
49 modelling methods (Hirakawa *et al.* 2003; Liu and Ling 2005; Ezzein *et al.* 2015; Hussein and Meguid
50 2016).

51 Modelling the behaviour of the soil-geosynthetic interface while taking into account the complex
52 mechanisms of interaction requires the performance of large-scale pullout or direct shear tests (Moraci
53 and Recalcati 2006; Moraci and Cardile 2008; Liu *et al.* 2009; Moraci and Cardile 2009; Palmeira
54 2009; Sieira *et al.* 2009; Dixon 2010; Cazzuffi *et al.* 2011; Moraci and Cardile 2012; Zhou *et al.* 2012;
55 Calvarano *et al.* 2014; Cardile *et al.* 2014; Cazzuffi *et al.* 2014; Ezzein and Bathurst 2014; Moraci *et*
56 *al.* 2014; Bathurst and Ezzein 2015; Cardile *et al.* 2016; Liu *et al.* 2016).

57 Using standard procedures (ISO 10319:2015, ASTM D 4595-11), in-isolation monotonic tensile tests
58 can characterise the tensile behaviour of geosynthetic inclusions under static conditions. However,
59 these standard tensile tests do not take into account the non-linear behaviour of geosynthetic materials
60 under cyclic or dynamic tensile load conditions, while the Standard ASTM D 7556-10 provides the
61 tensile stiffness of geogrids and geotextiles for applications involving small-strain cyclic loading.
62 Accumulation of permanent strain that occurs cycle-by-cycle under application of non-zero mean
63 tensile stress (ratcheting) is observed when cyclic tensile tests are performed. Generally, experimental
64 results show a hysteresis effect. Kinematic hardening concepts are typically used to explain ratcheting.
65 When the stress state reaches the yield surface, the surface must either grow, contract or shift with
66 loading and unloading.

67 Ashmawy and Bourdeau (1996) studied woven polyester (PET) and nonwoven polypropylene (PP)
68 geotextiles under monotonic and cyclic loading conditions. The results of the cyclic tensile tests were
69 different in terms of cyclic tensile behaviour between geosynthetics having different manufacturing
70 procedures (structure) and different constituent polymers.

71 Vieira and Lopes (2013) performed cyclic tests at a constant strain rate on a reinforcing geocomposite
72 in order to study the effects of strain rate (20% per min and 2% per min) by using a fixed unloading–
73 reloading history. The tested geocomposite consisted of PP continuous filament nonwoven geotextile,
74 reinforced with high-strength PET yarns. The loading strain rate did not particularly influence the
75 cyclic tensile load–strain behaviour, in terms of unload stiffness, reload stiffness and damping.

76 Moreover, the influence of frequency on residual strain was analysed by cyclic tensile tests (ten
77 unload–reload cycles) performed at a constant load rate. As in previous research, residual strain
78 decreased with increasing investigated loading frequency (0.001–0.02 Hz). In restarting (at the same
79 strain rate) the tensile test on the same specimen previously used in the cyclic load tests, the authors
80 observed no significant strength reduction with respect to the tests carried out on the virgin specimen.

81 Zanzinger *et al.* (2010) studied the fatigue behaviour of a PET geogrid under cyclic loading at
82 different high frequencies (3 Hz and 10 Hz) with a dynamic loading representative of train traffic. The
83 performed tensile tests showed that damage increases with increasing cyclic load frequency, as well as
84 with increasing maximum values of cyclic load.

85 A few researchers have investigated the cyclic tensile behaviour of high-density polyethylene (HDPE)
86 geogrids (Bathurst and Cai 1994; Moraci and Montanelli 1997; Ling *et al.* 1998; Kongkitkul *et al.*
87 2004), object of this research. HDPE is a semi-crystalline polymer and, as such, can be considered as
88 belonging to a two-phase continuum: a crystalline skeleton surrounded by meso-regions of chains in
89 the rubbery state (Drozdov and Christiansen 2007), which constitutes the amorphous phase. This
90 structural complexity leads geosynthetic materials to show thermo-visco-elastic-plastic and direction-
91 dependent behaviour.

92 Bathurst and Cai (1994) carried out cyclic tensile tests on HDPE and PET geogrid specimens. The
93 authors reported that the load frequency (0.1, 0.5, 1.0, 2.0 and 3.5 Hz) affects hysteretic behaviour
94 (mainly in HDPE geogrids, PET specimens being relatively insensitive), as well as the level of tensile
95 load.

96 Moraci and Montanelli (1997) drew the same conclusions after investigating the cyclic tensile
97 behaviour of HDPE and PET geogrids. The authors carried out cyclic tensile tests at different
98 frequencies (0.1, 0.25, 0.5 and 1 Hz) and different tensile load levels for durations up to 10000 cycles.
99 The results showed that tensile stiffness increases and damping decreases with increasing number of
100 cycles, agreeing with the results of Bathurst and Cai (1994). These studies confirm that there are
101 important creep effects for HDPE geogrids at lower frequencies. Moreover, in the range of applied
102 tensile loads generally used in designs, cyclic tensile tests conducted at the same level of load and
103 frequency showed that the ratio between the maximum cycle strain (ε_{tc}) and the monotonic tensile
104 strain (ε_{tm}) measured during a wide-width tensile test at the corresponding maximum level of load is a
105 function of the number of cycles:

$$106 \quad \varepsilon_{tc} = \varepsilon_{tm} (a + b \log N) \quad (1)$$

107 When the load level increases, the function changes, being non-linear in the ε_{tc} - $\log N$ semi-
108 logarithmic graph. For this reason, Ling *et al.* (1998) suggested using a hyperbolic relationship to
109 predict the cumulative strain during cyclic loadings.

110 All of the above-mentioned research has shown that the tensile strength of geogrids does generally not
111 degrade as a result of short-term cyclic loading.

112 Another investigation of the cyclic load-strain response of geosynthetic specimens of different
113 materials (HDPE, polyarylate and polyvinyl alcohol geogrids) was reported by Kongkitkul *et al.*
114 (2004). Within the limit of the low cyclic tensile load frequencies applied (0.01–0.2 Hz), this research
115 showed that the residual strains developed during cyclic loading were essentially due to the viscous
116 properties of the raw material. For these materials, the authors reported that the effects of cyclic
117 loading history are essentially controlled by the total period of cyclic loading, being very similar to
118 those occurring during a history of constant equivalent sustained load. Rate-independent cyclic
119 loading effects could be relevant when viscous effects are negligible.

120 To simulate the stress-strain-time behaviour of geosynthetics during cyclic tensile loading, some
121 authors (Perkins 2000; Kongkitkul *et al.* 2004; Liu and Ling 2007) developed non-linear models that
122 incorporate components describing direction-dependent elastic, plastic and time-dependent tensile
123 creep properties. These models roughly reproduce observations made during cyclic tensile loading, but
124 they are not perfectly suited for modelling damping behaviour.

125 In this context, this paper aims to expand the knowledge of the cyclic and post-cyclic tensile behaviour
126 of a HDPE extruded uniaxial geogrid by means of several monotonic and multistage wide-width
127 tensile tests.

128 For the parameters obtained during hysteresis loops, the influences of pre-stress tensile load P_i
129 (ranging from about 10% to 50% of maximum tensile strength), cyclic tensile loading amplitude A
130 (ranging from about 10% to 50% of maximum tensile strength), number of cycles N (1000 cycles) and
131 frequency ($f=0.01, 0.1, 1$ Hz) have been investigated in depth.

132 Multiple regression analyses performed on the test results have allowed the development of a
133 combined empirical model able to adequately predict the behaviour of a HDPE extruded geogrid
134 subject to cyclic loading histories (defined by a fixed pre-stress load, loading amplitude, frequency and
135 number of cycles), allowing the reinforcement's damping to be modelled when performing numerical
136 analyses of GSR structures.

137 Moreover, the difference between the maximum tensile strength of the tested geogrid as obtained by
138 monotonic and multistage tensile tests has been investigated.

139

140 **2 TEST MATERIAL AND MONOTONIC TENSILE TEST RESULTS**

141 Tensile tests were carried out on a geogrid (GGR1) provided by an Italian manufacturer, which
142 produced it from HDPE by means of an extrusion process. It is the uniaxial type, designed for
143 reinforcement use in one direction. Table 1 lists the geometric properties of the investigated geogrid.
144 Its mechanical behaviour was investigated by means of wide-width monotonic and multistage tensile
145 tests, using a tensile test apparatus (Figure 1a) controlled by a digital servo controller integrated with a
146 data acquisition system. The test equipment essentially comprises hydraulic clamps for gripping the
147 specimen (Figure 1b), a hydraulic test actuator–hydrostatic bearing (Figure 1c), the hydraulic unit and
148 its supply line (Figure 1d).

149 Monotonic tensile tests were performed on five specimens in the standard atmosphere for testing
150 ($20\pm2^{\circ}\text{C}$ at $65\pm5\%$ RH), as defined in ISO 554:1976, using index test procedures (ISO 10319:2015).
151 Each specimen was held across its entire width in the clamps set of the tensile test machine, operating
152 at a constant strain rate (CSR) equal to $\varepsilon'=20\%$ per minute, as recommended by the European
153 Standard.

154 The longitudinal force applied to the specimen until its rupture was measured by means of a load cell,
155 while the elongation measurements were made by an optical extensometer. The average values of the
156 maximum tensile strength per unit width, $T_{max(ISO)}$, the strain at maximum tensile strength, $\varepsilon_{max(ISO)}$, and
157 the secant tensile stiffness at 2% strain, $J_{sec\ 2\%(ISO)}$, were calculated.

158 Since the HDPE material exhibits strongly time-dependent behaviour—which means that stress
159 loading rates affect the tensile response—additional monotonic tensile tests at strain rates 100 times
160 lower than that required by ISO 10319:2015 ($\varepsilon'=0.2\%$ per minute) were carried out. The maximum
161 tensile strength per unit width, T_{max} , the strain at maximum tensile strength, ε_{max} , and the secant tensile
162 stiffness at 2% strain, $J_{sec\ 2\%}$, were obtained. The results show that, as expected, when the strain rate

163 decreases, the same value of tensile force is achieved for higher values of strain. Table 2 lists the
164 monotonic tensile test results at strain rates equal to 20% per min and 0.2% per min.

165

166 **3 MULTISTAGE TENSILE TEST PROCEDURE**

167 Cyclic tensile tests were carried out (at the same conditions of temperature and humidity as the
168 monotonic tests) using a multistage procedure (MS), Figure 2a, consisting of three steps (Moraci and
169 Cardile 2009, 2012):

170 a) a pre-stress stage at CSR equal to $\varepsilon'=0.2\%$ per minute, reaching a fixed tensile monotonic load P_i
171 chosen as T_{max} percentage;

172 b) a cyclic stage using a sinusoidal function, with a fixed, controlled tensile loading amplitude A
173 (chosen as T_{max} percentage) and frequency f , for 1000 cycles in total. Load-controlled conditions for
174 the cyclic tests simulate field conditions (i.e., a traffic load) better than do displacement-controlled
175 conditions, allowing the measurement of residual strains as a function of number of cycles N for a
176 given loading amplitude A (Ashmawy and Bourdeau 1996); and

177 c) a post-cyclic stage at CSR equal to $\varepsilon'=0.2\%$ per minute until specimen rupture occurs, which is
178 useful to verify the influence of the applied cyclic loading on geogrid tensile strength.

179 The MS tensile tests (20 in total) were carried out at the cyclic frequency $f=0.1$ Hz, ranging pre-stress
180 tensile load P_i from 6% to 50% of T_{max} and ranging cyclic tensile loading amplitude A from 8% to 52%
181 of T_{max} (Table 3). Moreover, additional tests (six in total) were performed in order to study the
182 influence of frequency ($f=0.01$ and 1 Hz), ranging cyclic tensile loading amplitude A from 21% to 52%
183 of T_{max} and for a fixed pre-stress tensile load $P_i \approx 33\%$ (Table 3). All specimens were tested along their
184 machine direction.

185

186 **4 ANALYSIS OF MULTISTAGE TENSILE TEST RESULTS**

187 The parameters obtained for each unload-reload cycle are: unload, reload and hysteretic stiffness (J_u ,
188 J_r , J_h , respectively); hysteretic area included in the hysteresis loops, A_{ur} ; residual strain caused by
189 cyclic loading, ε_r ; and maximum strain reached during each cyclic loading, ε_{rc} (Figure 2b).

190 For each of these parameters, the influence of pre-stress tensile load P_i , tensile loading amplitude A ,
191 number of cycles N and frequency f was investigated.

192 Results were analysed by identifying A/T_{max} and P_i/T_{max} classes (normalising A and P_i with respect to
193 the maximum tensile strength per unit width T_{max} obtained on the 0.2% per min CSR monotonic test)
194 within which these ratios are similar.

195

196 **4.1 Unload, reload and hysteretic stiffness**

197 Figure 3a shows the values of unload and reload stiffness (J_u, J_r) obtained for three of the MS tests
198 (tests T_{16}, T_{23} and T_{26} at equal values of $P_i/T_{max}=0.33$ and $A/T_{max}=0.52$ and at frequencies $f=0.1, 1$ and
199 0.01 Hz, respectively); these tests are qualitatively representative of all performed tests. The graph
200 reports the trend of J_u and J_r for varying number of loading cycles N on a logarithmic scale.

201 Differences in behaviour between these parameters can be summarised. For all the frequencies, in the
202 first 10 cycles J_u decreases with increasing number of loading cycles while J_r increases; exceeding this
203 ideal threshold, the two stiffnesses tend to merge into a single curve. Moreover, J_u and J_r increase with
204 increasing frequency; specifically, for J_u it is possible to record, for all the A/T_{max} investigated classes,
205 an increment equal to 20–40 % when the frequency increases from $f=0.01$ Hz to $f=0.1$ Hz and an
206 increment equal to 18–37 % when the frequency increases from $f=0.1$ Hz to $f=1$ Hz. In both cases, the
207 higher increments generally refer to lower numbers of cycles and higher normalised loading
208 amplitudes. The slopes of the J_u curve, in the first ten cycles, increase with increasing frequency.

209 For J_r the increments, for all the A/T_{max} investigated classes, are equal to 28–51 % when the frequency
210 increases from $f=0.01$ Hz to $f=0.1$ Hz and equal to 28–42 % when the frequency increases from $f=0.1$
211 Hz to $f=1$ Hz. In both cases, the higher increments refer to lower numbers of cycles.

212 The graph in Figure 3b shows the different behaviour of hysteretic stiffness with varying numbers of
213 loading cycles N on a logarithmic scale and for tests with equal, normalised pre-stress load
214 ($P_i/T_{max}\approx 0.33$), increasing normalised loading amplitude ($A/T_{max}=0.21, 0.31, 0.52$) and at different
215 frequencies ($f=0.01, 0.1, 1$ Hz). For $f\leq 0.1$ Hz, J_h increases with increasing number of cycles and, N
216 being equal, decreases with increasing A . This behaviour— J_h decreasing with increasing A —could be
217 explained by reference to the fact that the average strain rate remains quite low during all cycles, thus

218 not entailing increments of stiffness that are able to reverse the typical behaviour of the HDPE
219 material under constant test rate (i.e. decreasing stiffness with increasing loading level).
220 For $f=1$ Hz, the J_h curve exhibits the reverse behaviour during the first ten cycles, since it increases
221 with increasing normalised loading amplitude. In this case, during early cycles, with increasing A the
222 loading process occurs with enough increased average strain rate that stiffness also increases.
223 Exceeded the $N=10$ threshold, the trend is inverted because the average strain rate has reduced.
224 Thereafter, the geogrid follows the previously described behaviour.
225 In Figure 4a, it is possible to observe that the unload stiffness J_u , calculated at the cycle $N=1$ and for
226 $f=0.1$ Hz, generally decreases with increasing normalised loading amplitude A for each range of
227 normalised pre-stress load P_i within which this value is almost constant ($P_i/T_{max} \approx 0.12$, $P_i/T_{max} \approx 0.20$,
228 $P_i/T_{max} \approx 0.31$, $P_i/T_{max} \approx 0.49$). While, for a fixed normalised A value, J_u at $N=1$ increases with increasing
229 normalised pre-stress load P_i .
230 Figure 4b shows the unload stiffness J_u calculated at the cycle $N=10$ and for $f=0.1$ Hz versus the
231 normalised loading amplitude A for the different analysed classes of P_i/T_{max} . Even in this case, J_u
232 decreases with increasing normalised loading amplitude A for each range of normalised pre-stress load
233 P_i within which this value is almost constant. Compared with J_u values at $N=1$, J_u values at $N=10$ are
234 significantly lower, with differences ranging from 9% to 30%. The highest differences refer to the
235 highest investigated normalised P_i values.
236 J_u values at $N=1000$, for $f=0.1$ Hz, do not differ much from J_u values at $N=10$. In detail, there are slight
237 increments ranging from 0% to 8% (Figure 4c).
238 Figure 4d shows the reload stiffness J_r calculated at the cycle $N=1$ and for $f=0.1$ Hz versus the
239 normalised loading amplitude A for different analysed classes of P_i/T_{max} . The dependence of J_r values
240 at $N=1$ on A and P_i seems negligible, as J_r maintains constant values equal to 2600 kN/m on average.
241 In Figure 4e, it is possible to observe that the value of reload stiffness J_r calculated at the cycle $N=10$
242 and for $f=0.1$ Hz exhibits a slight but clear decrease with increasing normalised loading amplitude A .
243 In addition, for a given A/T_{max} value, J_r at $N=10$ increases with increasing normalised pre-stress load
244 P_i . The J_r values at $N=10$ are higher than those calculated at the cycle $N=1$, increments ranging from
245 53% to 101%.

246 J_r values at $N=1000$ do not differ much from those at $N=10$; there are slight increments ranging from
247 0% to 15% (Figure 4f).

248

249 **4.2 Hysteretic area**

250 Figure 5a, referring to $f=0.1$ Hz, shows results in terms of the hysteretic area A_{ur} with varying N on a
251 logarithmic scale for all performed tests grouped by constant A/T_{max} classes within which the P_i/T_{max}
252 ratio varies. When the normalised loading amplitude is low, it is possible to observe that the hysteretic
253 area A_{ur} remains almost constant over all loading cycles. By contrast, when the normalised loading
254 amplitude increases, A_{ur} increases for the first ten loading cycles and then decreases. Specifically, the
255 area of the hysteresis loops is approximately zero for values of loading amplitude lower than about
256 10% of T_{max} ; in other words, the specimen exhibits elastic linear behaviour with fully recoverable
257 strain. These results agree with those of Bathurst and Cai (1994).

258 The influence of frequency on A_{ur} has also been investigated. Figure 5b shows the hysteretic area A_{ur}
259 obtained for three of the MS tests (T_{16} , T_{23} , T_{26}) at equal values of $P_i/T_{max}=0.33$ and $A/T_{max}=0.52$ and
260 frequencies $f=0.1$, 1 and 0.01 Hz, respectively. These tests are qualitatively representative of all
261 performed tests. The graph shows the trend in A_{ur} for varying number of loading cycles N on a
262 logarithmic scale. A_{ur} increases with decreasing frequency, showing average increments equal to 34–
263 43% when the frequency decreases from $f=0.1$ Hz to $f=0.01$ Hz and average increments equal to 49–
264 88% when the frequency decreases from $f=1$ Hz to $f=0.1$ Hz. In both cases, the higher increments refer
265 to lower numbers of cycles.

266

267 **4.3 Cyclic residual and maximum strains**

268 In agreement with Figure 2b, the residual strain ε_r is defined as the cumulative deformation mobilised
269 in the specimen at the end of each corresponding cycle (when the tensile cyclic load returns to the
270 value of pre-stress load P_i).

271 The graph in Figure 6a, referring to $f=0.1$ Hz, shows the residual strain ε_r for varying N on a
272 logarithmic scale for all performed tests grouped by constant A/T_{max} classes within which the P_i/T_{max}

ratio varies. It is possible to observe that the residual strain ε_r increases with increasing numbers of cycles and normalised loading amplitude A , its trend becoming less and less linear. Moreover, for the lower A/T_{max} classes, ε_r seems scarcely dependent on the normalised pre-stress load P_i during the early loading cycles, but when the number of cycles increases, this dependence becomes evident, appearing to be much more significant with higher loading amplitudes. Considering the first loading cycle, ε_r ranges from 0.1% to 1.3%; at $N=10$, ε_r ranges from 0.2% to 3.0%; at $N=100$, ε_r ranges from 0.4% to 5.0%; and at $N=1000$, ε_r ranges from 0.5% to 8.3%.

Regarding the influence of frequency, Figure 6b shows ε_r obtained for three of the MS tests (T_{16} , T_{23} , T_{26} at equal values of $P_i/T_{max}=0.33$ and $A/T_{max}=0.52$ and frequencies $f=0.1$, 1 and 0.01 Hz, respectively), which are qualitatively representative of all performed tests. For the different investigated A/T_{max} classes, ε_r increases with decreasing frequency, recording increments equal to 24-173 % when the frequency decreases from $f=0.1$ Hz to $f=0.01$ Hz and increments equal to 0-110 % when the frequency decreases from $f=1$ Hz to $f=0.1$ Hz. In both cases, the higher values refer to lower number of cycles and lower normalised loading amplitudes. For a fixed number of cycles, the different accumulation of strain at different frequencies is due to the very different loading times. The strain component caused by creep obviously increases with increasing loading time. Moreover, looking at the trend, it is possible to observe that the curve at $f=0.01$ Hz is concave downward, the slope decreasing with increasing number of cycles. By contrast, the opposite trend is observed for the curve at $f=1$ Hz, which is concave upward until $N=100$, after which it returns downward. This phenomenon could be explained by considering that the increments of residual strain will disappear with increasing number of cycles, reaching a sort of ideal steady state.

The graph in Figure 7a shows the maximum strain ε_{ic} , for varying N on a logarithmic scale, for all performed tests at $f=0.1$ Hz grouped by constant A/T_{max} classes within which the P_i/T_{max} ratio varies. The maximum strain ε_{ic} increases with increasing numbers of cycles and normalised loading amplitude A and, for a fixed constant A/T_{max} class, ε_{ic} increases with increasing normalised pre-stress load P_i . By contrast to the observation for residual strain (Figure 6a), the trend in maximum strain is

299 generally linear in the semi-logarithmic graph; only in cases where the combined values of A ($A \approx 0.50$
300 T_{max}) and P_i ($P_i = 0.51 T_{max}$) reach the maximum tensile strength T_{max} does it significantly deviate from
301 linearity. This trend confirms the results of the experimental studies carried out by Moraci and
302 Montanelli (1997).

303 In the current experimental study, the maximum strain, ε_{tc} , and the tensile strain, ε_{tm} , measured during
304 the 0.2% per min CSR monotonic test at the corresponding cycle maximum load, were compared. The
305 trend in the ratio $\varepsilon_{tc}/\varepsilon_{tm}$ for varying numbers of loading cycles N is plotted for all performed tests at
306 $f=0.1$ Hz, grouped by constant A/T_{max} classes within which the P_i/T_{max} ratio varies (Figure 7b), as well
307 as for three of the MS tests at different frequencies (T_{16} , T_{23} , T_{26} at equal values of $P_i/T_{max}=0.33$ and
308 $A/T_{max}=0.52$ and frequencies $f=0.1$, 1 and 0.01 Hz, respectively; Figure 7c). Within the investigated
309 values, the trend is linear as plotted on the semi-logarithmic graph; following Moraci and Montanelli
310 (1997), this trend can be very accurately described by the logarithmic regression (1).

311 This result allows the calculation of maximum strain ε_{tc} after N loading cycles for a specific cyclic
312 loading amplitude and frequency just by carrying out monotonic tensile tests at a constant rate of
313 strain. Equation (1) is valid only for investigated A and P_i values, for which it closely approximates the
314 experimental data ($P_i/T_{max} < 0.51$ and $A/T_{max} < 0.52$).

315

316 **4.4 Tensile strength**

317 The difference between the tensile load-strain relations for the 0.2% per min CSR monotonic test and
318 those for the MS tests has also been investigated in order to verify the influence of cyclic load on the
319 maximum tensile strength. This comparison is reported in Figure 8a for the MS test T_{18} ($P_i/T_{max}=0.46$,
320 $A/T_{max}=0.47$); this test is qualitatively representative of all those performed.

321 With respect to the MS curve, there is a sudden change in tensile stiffness passing from the first stage,
322 wherein the test rate is constant and low, to the second stage, in which the test rate is considerably
323 higher in order to ensure the intended loading amplitude. Since HDPE is a visco-plastic material, such
324 differences in test rates affect tensile load-strain curves in terms of stiffness.

325 Finally, when the post-cyclic stage starts, the tensile load–strain relation exhibits very high tensile
326 stiffness, despite the lower test rate (0.2% per min CSR), until the monotonic reference curve is re-
327 joined. Therefore, cyclic deformation is not a phenomenon of material degradation because the effects
328 of cyclic loading histories disappear once the load again starts to increase.

329 Figure 8b illustrates the maximum tensile strength per unit width $T_{max(MS)}$ obtained in all MS tests
330 (normalised with respect to T_{max}) for varying the normalised loading amplitude A and for different
331 ranges of normalised pre-stress load P_i . A very small increase in strength with increasing loading
332 amplitude A can be observed; this behaviour could be explained by reference to the increased strain
333 rate during cyclic stages carried out at the same frequency. However, these differences appear to be
334 insignificant and comparable with the production variability of the materials, as they are always
335 positive and lower than 6%. Moreover, the pre-stress load levels do not seem to significantly affect the
336 results. Therefore, the results for the hyperbolic trend suggest that cyclic loading histories do not
337 induce a reduction in geosynthetic tensile strength, agreeing with the results of Kongkitkul *et al.*
338 (2004) and Vieira and Lopes (2013).

339

340 **5 COMBINED MODEL FOR PREDICTING GEOGRID TENSILE BEHAVIOUR UNDER 341 CYCLIC LOADINGS**

342 The experimental results have suggested that the tensile behaviour of a HDPE geogrid subject to
343 monotonic and cyclic loading histories is strongly dependent on several parameters. Any predictive
344 model must be able to account for all of them.

345 From the damping definition expressed in Figure 2b, the following equation for the reinforcement's
346 damping is obtained:

$$347 D = \frac{A_{ur}}{\pi J_h (\varepsilon_{tc} - \varepsilon_r)^2} \quad (2)$$

348 This allows modelling geogrids when numerical analyses of GSR structures are performed. The
349 possibility of modelling the reinforcement's damping leads to numerical analyses that better predict
350 displacements of GRS structures. Numerical modelling performed by Mendonca and Lopes (2011)

351 highlighted that the maximum horizontal seismic displacement of a soil embankment reinforced with
 352 HDPE geogrids and subject to harmonic acceleration is dependent on damping of both soil and the
 353 reinforcement, demonstrating the importance of having in-air experimental results on geosynthetics
 354 under cyclic loading.

355 Several empirical relationships predicting the terms in (2) have been developed, taking specifically
 356 into account:

- 357 - the pre-stress tensile load P_i and the maximum tensile strength per unit width T_{max} reached at
 358 CSR equal to $\varepsilon'=0.2\%$ per min, representative of serviceability conditions under monotonic
 359 tensile loading; and
 360 - the tensile loading amplitude A , the frequency f and the number of cycles N , which
 361 characterise a specific cyclic loading history.

362 The proposed empirical models were formulated using a multiple regression procedure on all
 363 experimental data, resulting in the expressions shown below for hysteretic stiffness (3), area of
 364 hysteresis loops (4) and residual strains (5), valid over the range of analysed values:

$$365 J_h = \left(296 \frac{P_i}{T_{max}} - 141 \frac{A}{T_{max}} + 90 \right) \log N + \left[\frac{2314 \frac{P_i}{T_{max}} - 2270 \frac{A}{T_{max}} [(0.30 \log N - 1.51)f + 0.95] + 4351}{\left(\frac{-0.006f + 0.001}{0.13f + 0.04} \right) \log N + \frac{0.12f + 0.005}{0.14f + 0.003}} \right] \quad (3)$$

$$366 A_{ur} = \left[\frac{\left(e^{\frac{A/T_{max}}{0.18}} - 1 \right) \cdot (1 - \log f) \cdot (3 \log N + 1)}{(6 \log N + 7.74f + 2.61)} \right] \cdot \left[\left(\frac{-1.71 \log N - 1.71}{3.12 \log N + 1} \right) \cdot \frac{P_i}{T_{max}} - 0.20 \log N + 1.62 \right] \quad (4)$$

$$367 \varepsilon_r = \left\{ \frac{\left[\frac{(0.16 \log N + 0.98)f + 0.25}{(4.40 - 0.45 \log N)f + 0.1} \right] \cdot (3.80 \log N + 2.86) \cdot \frac{A}{T_{max}}}{\left[\left(\frac{0.01f + 0.1}{2.18f + 0.07} \right) \log N + \left(\frac{1 - 41.39f}{1 + 84.37f} \right) \right] \cdot \frac{A}{T_{max}} + 1} \right\} \cdot \left[\frac{\left(\frac{1.90 \frac{P_i}{T_{max}} - 0.6}{3.95 \frac{P_i}{T_{max}} + 1} \right) + \left(2.89 \frac{P_i}{T_{max}} - 0.94 \right) \log N}{\log N + 1} + 1 \right]$$

368 (5)

369

370 With regard to the maximum strains, the a and b coefficients of the logarithmic regression (1) were
 371 calibrated, obtaining the following empirical regression:

372

$$373 \quad \varepsilon_{tc} = \varepsilon_{tm} \cdot \left\{ \begin{array}{l} 0.16 \log(N) + \\ + \frac{\left[\frac{0.39 - 0.52 \log f}{1 - 0.87f} - \left(\frac{0.16 + 0.16 \log f}{1 - 0.73f} \right) \cdot \log N \right]}{\left[\left\{ -22.04 \left(\frac{P_i}{T_{max}} \right)^2 + 14.60 \frac{P_i}{T_{max}} - 0.82 \right] + \left[\frac{0.66 - 0.25 \log f}{1 - 0.97f} - \left(\frac{1.03 + 1.03 \log f}{1 - 0.79f} \right) \cdot \log N \right] \cdot \frac{A}{T_{max}} \cdot \left[74.80 \left(\frac{P_i}{T_{max}} \right)^2 - 50.93 \frac{P_i}{T_{max}} + 9.26 \right] \right\}} \end{array} \right\}$$

374 (6)

375

376 The regression equations (3), (4), (5) and (6) are valid for the HDPE geogrid tested, its stiffness being
 377 right inside the numerical coefficients, therefore other tests are necessary to calibrate them for
 378 different geogrids. However, the regression equations could be helpful if GRS structures are designed
 379 with HDPE reinforcement having similar geometric and tensile properties. For fixed pre-stress load,
 380 loading amplitude and frequency values, equation (2) combined with (3), (4), (5) and (6) provides the
 381 geogrid's stiffness and damping with varying number of cycles (i.e. time). These results could be used
 382 for instance in the dynamic response analysis of a GRS structure, modelling it as a multi degree of
 383 freedom (M-DOF) system subject to base excitation and considering the geogrids contribution to
 384 elastic and viscous forces in the equations of motion. The mathematical model can be numerically
 385 solved using a step-by-step integration algorithm, updating also the stiffness and damping values.
 386 Clearly even the contribution representing soil-geosynthetic interface should be updated step-by-step,
 387 using results from large-scale pullout or direct shear tests under cyclic loading.

388 The Root Mean Square Error (RMSE) for all curves was evaluated, calculating the magnitudes of the
 389 errors between the values predicted by the model and those actually observed. Overall, all empirical
 390 models make good predictions of the experimental results. The parameters obtained using the
 391 proposed models are compared with the experimental results in the following figures.

392 Figure 9 shows the predicted (dashed lines) and experimental (symbols) values for hysteretic stiffness
393 referring to a specific loading cycle—(a) $N=1$, (b) $N=10$, (c) $N=100$ and (d) $N=999$ —and $f=0.1$ Hz
394 versus the normalised loading amplitude A for the different analysed classes of P_i/T_{max} . The same
395 behaviour can be observed in all loading cycles, with J_h generally decreasing with increasing
396 normalised loading amplitude A .

397 Figure 10 illustrates the predicted and experimental values for hysteretic stiffness with varying
398 normalised loading amplitude at different frequencies for a fixed, normalised pre-stress load class
399 ($P_i/T_{max}\approx 0.31$). The graphs refer to loading cycle (a) $N=1$, (b) $N=10$ and (c) $N=100$. The empirical
400 model is able to reproduce the specific behaviour observed for higher frequencies at lower numbers of
401 cycles that is highlighted in Figure 3b.

402 Figure 11 shows the hysteretic area A_{ur} obtained using the proposed model and that obtained in the
403 experimental results referring to specific loading cycles—(a) $N=1$, (b) $N=10$, (c) $N=999$ —and $f=0.1$
404 Hz versus normalised loading amplitude A for different analysed classes of P_i/T_{max} . The trend suggests
405 that A_{ur} exponentially increases with increasing normalised loading amplitude A , thus producing
406 decreasing stiffness as has previously been well-modelled; furthermore, for the lowest investigated
407 loading amplitudes, A_{ur} seems to be only slightly dependent on pre-stress load level, while it decreases
408 with increasing normalised pre-stress load P_i for higher A/T_{max} .

409 The predicted and experimental values of hysteretic area with varying normalised loading amplitude,
410 for a fixed, normalised pre-stress load class ($P_i/T_{max}\approx 0.31$) and at different frequencies are reported in
411 Figure 12 for numbers of loading cycles (a) $N=1$, (b) $N=10$ and (c) $N=100$.

412 Figure 13 shows the residual strains obtained using the proposed model and the experimental results
413 versus normalised loading amplitude for different loading cycles and at normalised pre-stress load
414 classes (a) $P_i/T_{max}\approx 0.12$, (b) $P_i/T_{max}\approx 0.20$, (c) $P_i/T_{max}\approx 0.31$ and (d) $P_i/T_{max}\approx 0.49$. All the graphs in this
415 figure refer to $f=0.1$ Hz.

416 Figure 14 shows the predicted and experimental values of residual strains with varying normalised
417 loading amplitude at different frequencies and for a fixed, normalised pre-stress load class
418 ($P_i/T_{max}\approx 0.31$). The graphs refer to numbers of loading cycles (a) $N=1$, (b) $N=10$ and (c) $N=100$.

419 The empirical model for residual strain makes good predictions of the various trends at varying
420 frequencies: the curve at $f=0.01$ Hz is concave downward, while at $f=1$ Hz the curve is the opposite
421 (concave slightly upward). The curve trend at $f=0.1$ Hz seems to be linear for lower classes of P_i/T_{max} ,
422 becoming less and less linear with increasing normalised pre-stress load.
423 Figure 15 shows the $\varepsilon_{tc}/\varepsilon_{tm}$ ratios obtained using the proposed model and the experimental results
424 versus normalised loading amplitude for different loading cycles and at normalised pre-stress load
425 classes (a) $P_i/T_{max} \approx 0.12$, (b) $P_i/T_{max} \approx 0.20$, (c) $P_i/T_{max} \approx 0.31$ and (d) $P_i/T_{max} \approx 0.49$. All graphs refer to
426 $f=0.1$ Hz. Figure 16 shows the predicted and experimental values of the $\varepsilon_{tc}/\varepsilon_{tm}$ ratio with varying
427 normalised loading amplitude at different frequencies and for a fixed, normalised pre-stress load class
428 ($P_i/T_{max} \approx 0.31$). The graphs refer to numbers of loading cycles (a) $N=1$, (b) $N=10$ and (c) $N=100$.
429 Comparing the experimental and predicted results clearly shows that the proposed combined model
430 well reproduces the cyclic tensile behaviour of the investigated geogrid.

431

432 **6 CONCLUSIONS**

433 Several monotonic and multistage wide-width tensile tests have been performed in order to improve
434 knowledge of the cyclic and post-cyclic tensile behaviour of a HDPE extruded uniaxial geogrid. The
435 viscous characteristics of HDPE affect the material's response. The influence of pre-stress tensile load
436 P_i , cyclic tensile loading amplitude A , number of cycles N and frequency f on the parameters obtained
437 during hysteresis loops has been investigated, leading to the following considerations:

- 438 1) At lower frequencies, hysteretic stiffness J_h increases with increasing number of cycles N ; if
439 N is equal, it decreases with increasing normalised loading amplitude. J_h decreasing with
440 increasing A could be explained by reference to the fact that the average strain rate remains
441 quite low during all cycles, thus not entailing increments of stiffness that are able to reverse
442 the typical behaviour of the HDPE material under constant test rate. For higher frequencies,
443 during early cycles, with increasing A the loading process occurs with enough increased
444 average strain rate that stiffness also increases. Exceeded the $N=10$ threshold, the trend is
445 inverted because the average strain rate has reduced.

- 446 2) J_u decreases with increasing number of loading cycles for the first 10 cycles, while J_r
447 increases; exceeding this ideal threshold, the two stiffnesses tend to merge into a single
448 curve (which is coincident with the J_h curve). For $f=0.1$ Hz, J_u and J_r generally decrease
449 with increasing normalised loading amplitude A , for each range of normalised pre-stress
450 load P_i within which this value is almost constant. For a given value of A/T_{max} , J_u and J_r
451 generally increase both with increasing normalised pre-stress load P_i and with increasing
452 frequency.
- 453 3) Referring to $f=0.1$ Hz, at the lower investigated loading amplitudes the hysteretic area A_{ur}
454 remains almost constant across all loading cycles. With increasing normalized loading
455 amplitude levels, by contrast, A_{ur} increases during the first ten loading cycles and then
456 decreases. For normalised loading amplitudes lower than 10% of T_{max} , the area of the
457 hysteresis loops is approximately zero, indicating the elastic behaviour of the material. For
458 $A/T_{max}>0.1$, A_{ur} begins to assume exponentially higher values (slightly dependent on the
459 normalised pre-stress load), which indicates the geogrid's plastic behaviour. Moreover, A_{ur}
460 decreases with increasing frequency.
- 461 4) With regard to residual strains, different behaviours were observed with varying
462 frequencies. The curve ε_r-N at $f=0.01$ Hz is concave downward, the slope decreasing with
463 increasing number of cycles. By contrast, the opposite trend is observed for the curve at $f=1$
464 Hz, which is concave upward until $N=100$ before turning downward. This condition might
465 be explained by considering that the increments of residual strain seem to disappear with
466 time, reaching a sort of ideal, stationary cyclic state.
- 467 5) For $f=0.1$ Hz, the residual strain ε_r increases with increasing number of cycles and
468 normalised loading amplitude A , its trend becoming less and less linear in the lin-log graph
469 $\varepsilon_r-\log N$. For lower A/T_{max} classes, ε_r seems hardly at all dependent on the normalised pre-
470 stress load P_i during early loading cycles, but this dependence becomes evident as the
471 number of cycles increases, appearing much more significant with higher loading
472 amplitudes. Moreover, ε_r increases with decreasing frequency. For a fixed number of

473 cycles, the different accumulation of strain at different frequencies is due to the very
474 different loading times. The strain component caused by creep obviously increases with
475 increasing loading time.

- 476 6) Maximum strain ε_{tc} increases with increasing number of cycles and normalised loading
477 amplitude A and, for a fixed, constant A/T_{max} class, ε_{tc} increases with increasing normalised
478 pre-stress load P_i . The trend in maximum strain is generally linear on the semi-logarithmic
479 graph $\varepsilon_{tc}-\log N$; only in cases where $A+P_i \approx T_{max}$ does it significantly deviate from linearity.

480 By following Moraci and Montanelli (1997) logarithmic regression,

481
$$\varepsilon_{tc} = \varepsilon_{tm} (a + b \log N)$$
, it is possible to obtain ε_{tc} after N loading cycles for a specific
482 cyclic load amplitude and frequency just by performing monotonic tensile tests at a constant
483 rate of strain. The a and b coefficients for the investigated geogrid are provided in the
484 current paper.

- 485 7) Cyclic loading histories do not induce reduced geosynthetic tensile strength.
486 8) Finally, a combined empirical model that well-predicts the tensile behaviour of the geogrid
487 under cyclic loadings was developed using a multiple regression procedure on all
488 experimental results, which allows modelling the damping of reinforcements when
489 performing numerical analyses of GSR structures.

490

List of notation

A	Cyclic tensile loading amplitude (kN/m)
A_{ur}	Hysteretic area included in the hysteresis loops (kN/m)
B_R	Node thickness (mm)
B_T	Thickness of the bar portion between two nodes (mm)
D	Damping (dimensionless)
ε_{max}	Tensile strain for T_{max} (monotonic test at 0.2% per min strain rate) (%)
$\varepsilon_{max(ISO)}$	Tensile strain for T_{max} (monotonic test at 20% per min strain rate, STANDARD ISO 10319) (%)
ε_r	Residual strain caused by cyclic loading (%)
ε_{tc}	Maximum strain reached during each cyclic loading (%)
ε_m	Tensile strain measured during the 0.2% per min strain rate monotonic test at the corresponding cycle maximum load (%)
ε'	Strain rate (% per min)
f	Frequency of cyclic load (Hz)
GGR1	Extruded Geogrid used in the current research
$J_{sec\ 2\%}$	Secant tensile stiffness at 2% strain (0.2% per min strain rate) (kN/m)
$J_{sec\ 2\%(ISO)}$	Secant tensile stiffness at 2% strain (20% per min strain rate, STANDARD ISO 10319) (kN/m)
J_h	Hysteretic stiffness (stiffness of the hysteresis loop, multistage test) (kN/m)
J_r	Reload stiffness (stiffness of the reload path, multistage test) (kN/m)
J_u	Unload stiffness (stiffness of the unload path, multistage test) (kN/m)
P_i	Pre-stress tensile load in monotonic conditions (kN/m)
S	Spacing between geogrid bearing members (mm)
T_{max}	Maximum tensile strength per unit width (monotonic test at 0.2% per min strain rate) (kN/m)
$T_{max(ISO)}$	Maximum tensile strength per unit width (monotonic test at 20% per min strain rate, STANDARD ISO 10319) (kN/m)
$T_{max(MS)}$	Maximum tensile strength per unit width (multistage test) (kN/m)
W_B	Width of the bar (mm)
W_R	Node width (mm)
W_T	Width of the bar portion between two nodes (mm)

492 **Tables**493 *Table 1. Geometric properties of the geogrid used in this research.*

Geogrid	Structure	S [mm]	W_T [mm]	B_T [mm]	W_R [mm]	B_R [mm]	W_B [mm]
GGR1	Extruded uniaxial	220	4.2	4.9	14.1	6.8	17.3

494

495

496 Table 2. Monotonic tensile test results at strain rates equal to 20% per min and 0.2% per min.

$T_{max(ISO)}$ [kN/m] ($\dot{\varepsilon}'=20\%$ per minute)	T_{max} [kN/m] ($\dot{\varepsilon}'=0.2\%$ per minute)	$\mathcal{E}_{max(ISO)} [\%]$ ($\dot{\varepsilon}'=20\%$ per minute)	$\mathcal{E}_{max} [\%]$ ($\dot{\varepsilon}'=0.2\%$ per minute)	$J_{sec\ 2\%(ISO)}$ [kN/m] ($\dot{\varepsilon}'=20\%$ per minute)	$J_{sec\ 2\%}$ [kN/m] ($\dot{\varepsilon}'=0.2\%$ per minute)
159.0	103.5	12.2	14.5	2454	1525

497

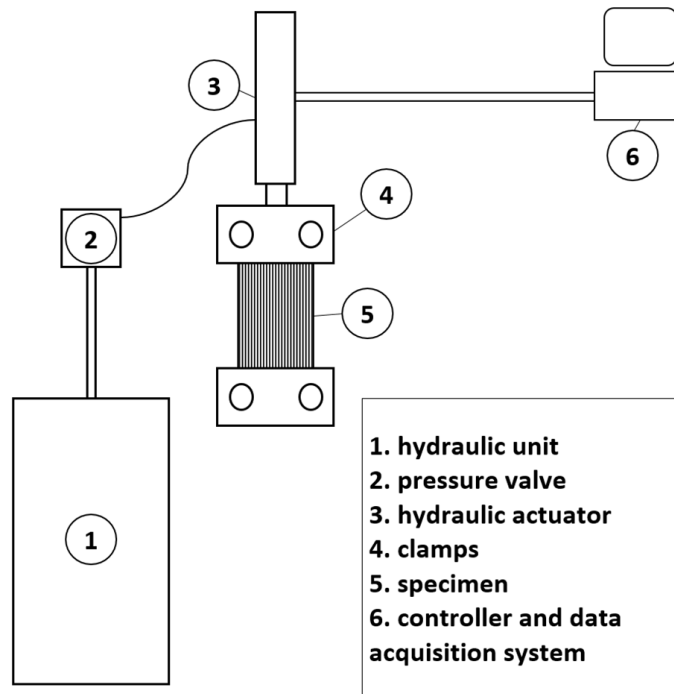
498

499 *Table 3. Testing plan.*

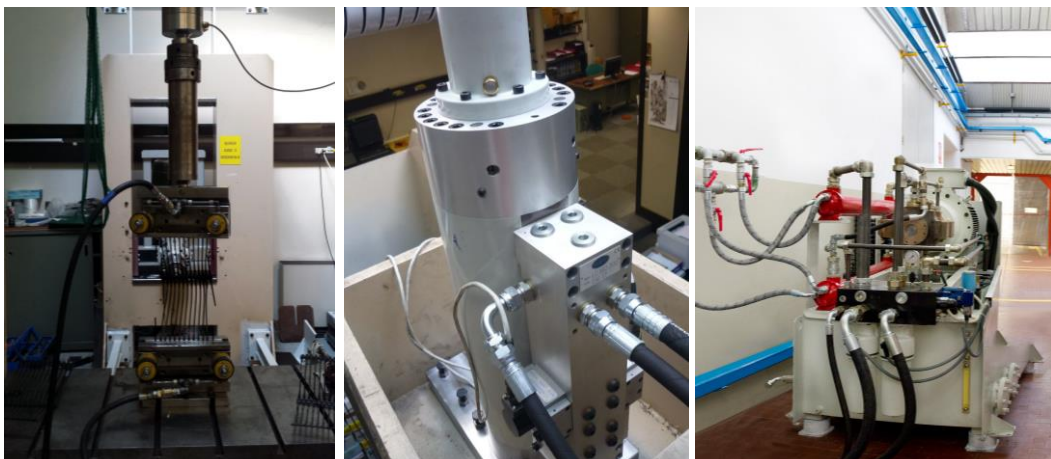
Test	P_i [kN/m]	P_i/T_{max} [%]	A [kN/m]	A/T_{max} [%]	f [Hz]
T01	6.28	6	7.96	8	0.1
T02	6.97	7	12.95	13	0.1
T03	10.94	11	7.85	8	0.1
T04	11.42	11	12.94	13	0.1
T05	13.62	13	13.54	13	0.1
T06	13.13	13	22.36	22	0.1
T07	21.26	21	13.52	13	0.1
T08	19.92	19	22.37	22	0.1
T09	19.53	19	21.21	20	0.1
T10	21.75	21	35.37	34	0.1
T11	30.74	30	29.44	28	0.1
T12	30.24	29	48.84	47	0.1
T13	34.44	33	21.14	20	0.1
T14	33.15	32	35.41	34	0.1
T15	33.55	32	32.21	31	0.1
T16	34.17	33	53.61	52	0.1
T17	47.17	46	29.42	28	0.1
T18	47.64	46	48.95	47	0.1
T19	52.72	51	32.22	31	0.1
T20	52.32	51	53.60	52	0.1
T21	33.93	33	22.14	21	1
T22	33.54	32	33.53	32	1
T23	33.72	33	55.04	53	1
T24	34.16	33	21.74	21	0.01
T25	32.15	31	32.18	31	0.01
T26	34.35	33	53.71	52	0.01

502 **Figures**

503



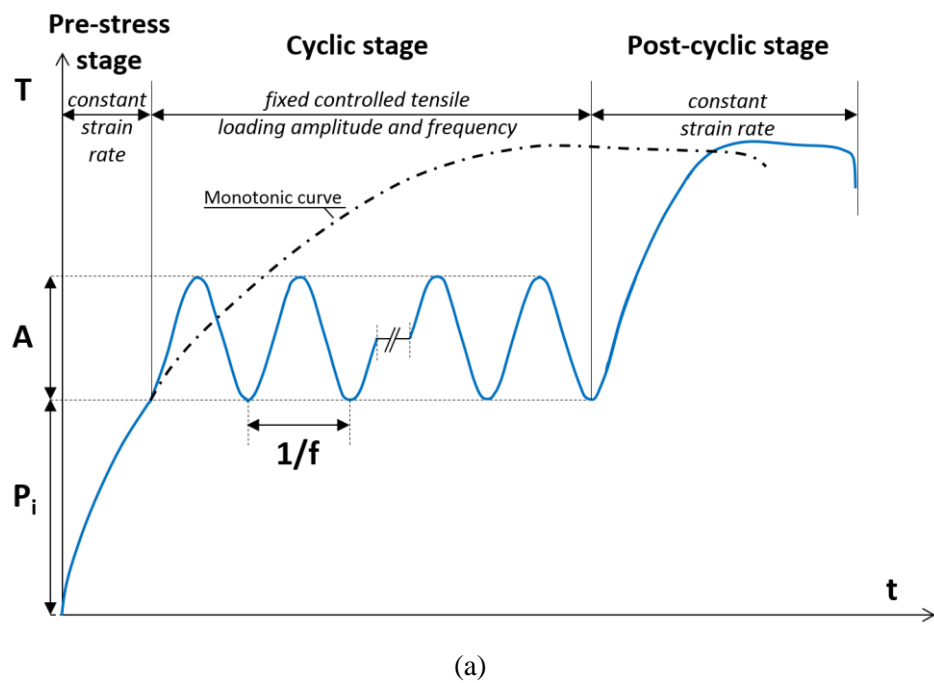
(a)



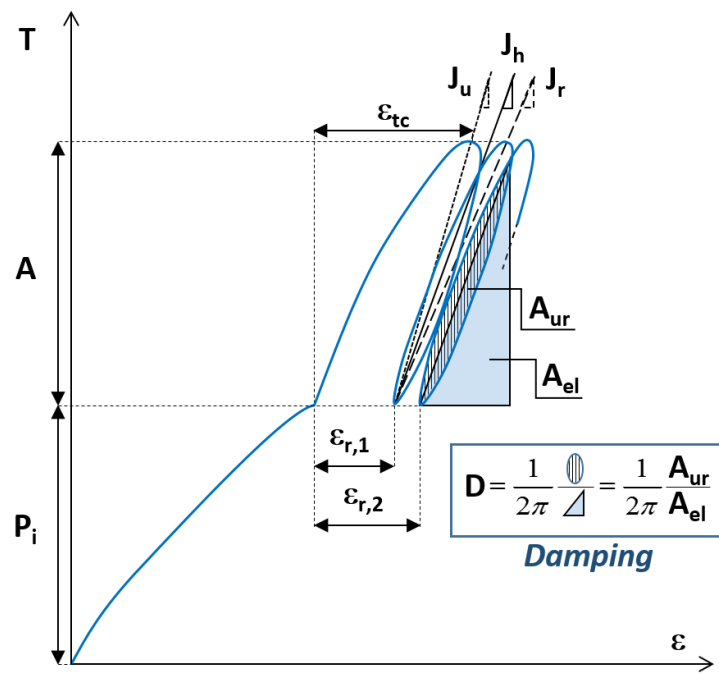
504

505 *Figure 1. Scheme of the equipment used for tensile testing the geogrid specimen (a); in detail:*
506 *hydraulic clamps (b); hydrostatic bearing actuator (c); hydraulic unit (d).*

507

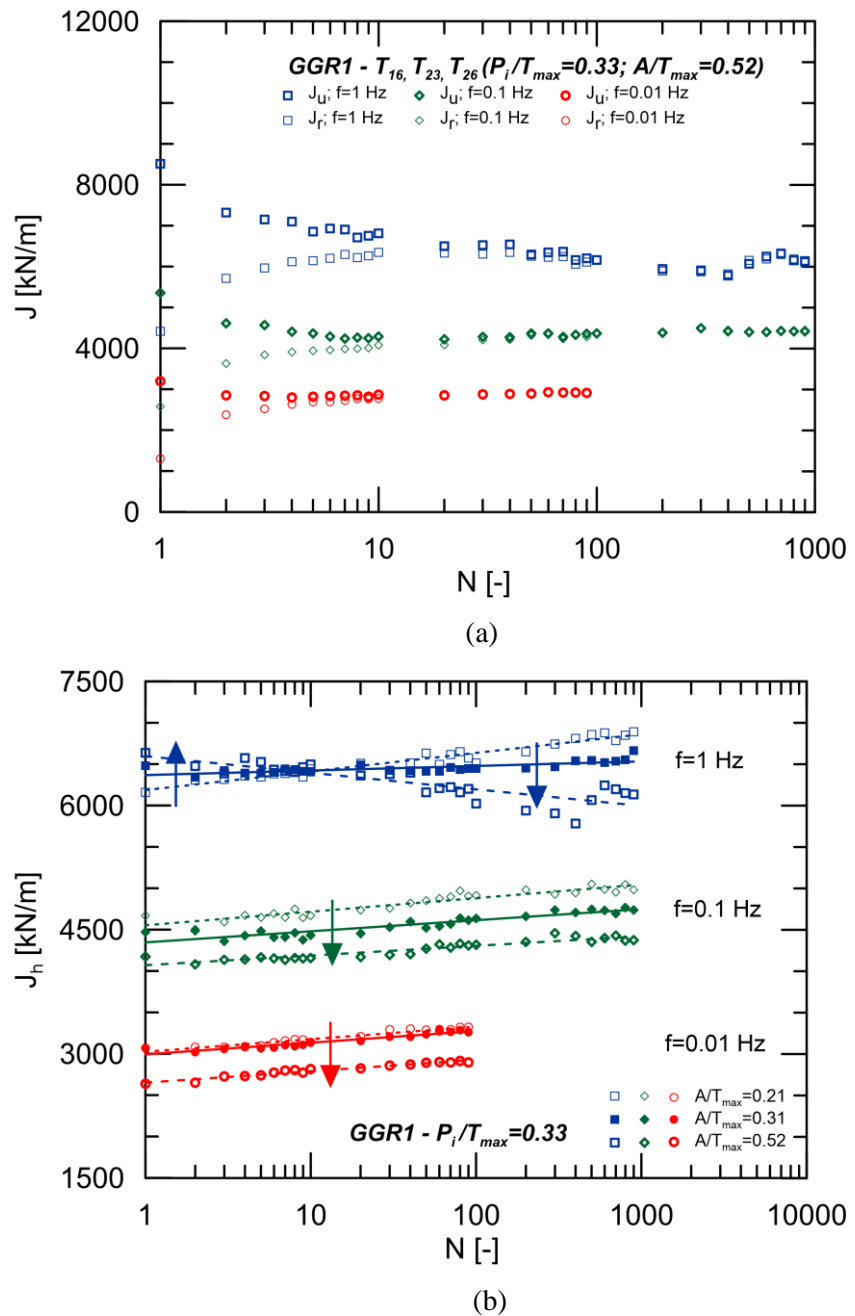


(a)



(b)

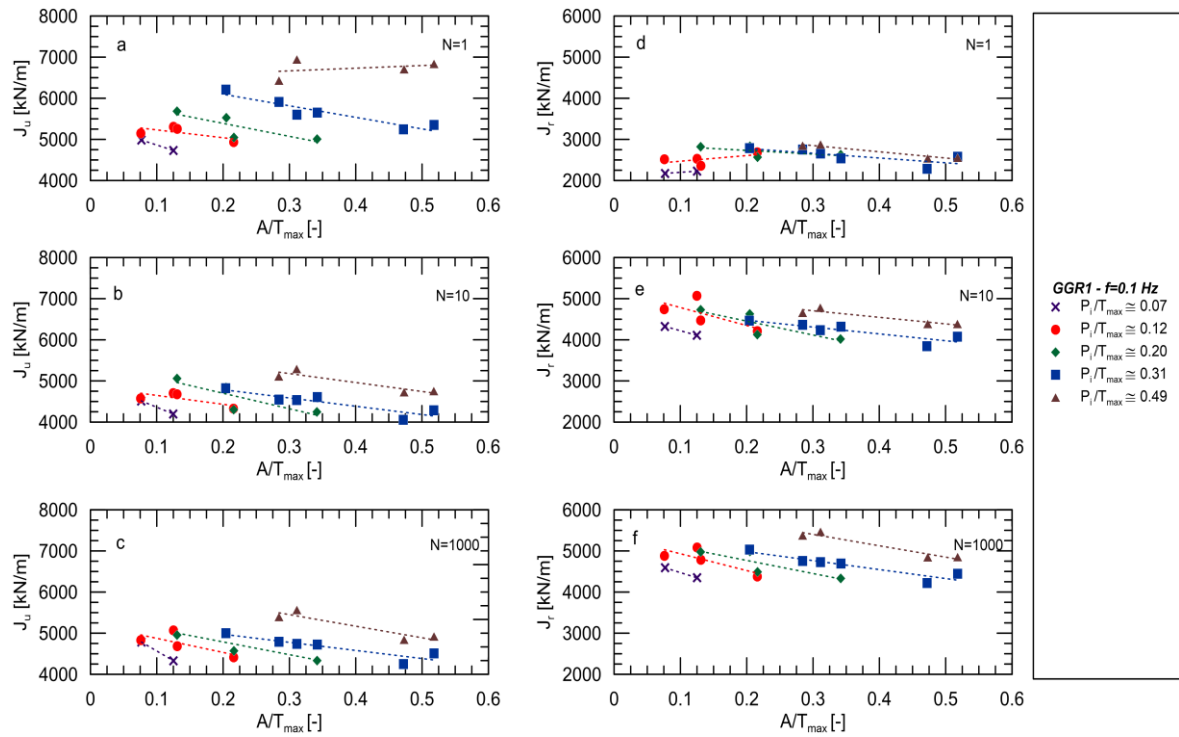
510 *Figure 2. Multistage procedure (a) and schematic representation of different parameters obtained
511 during hysteresis loops in multistage tests (b).*



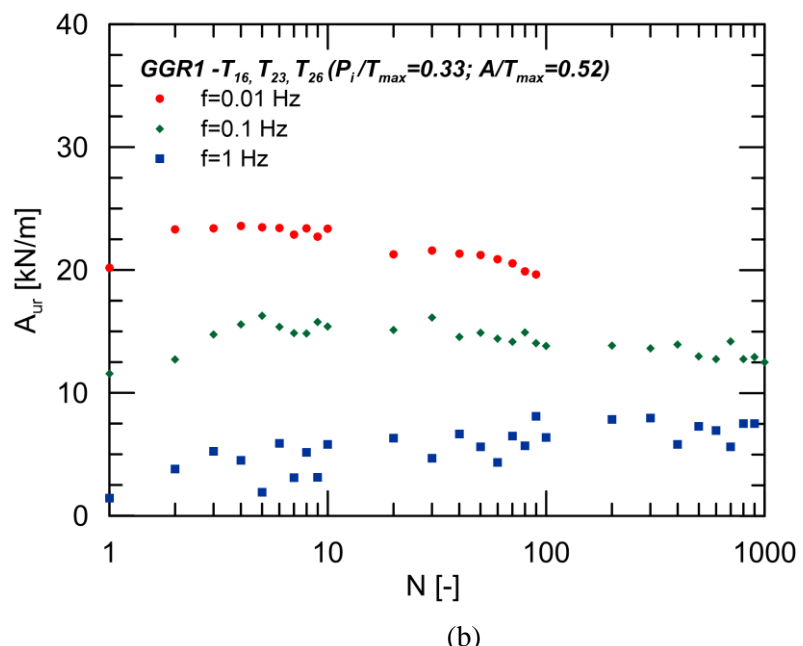
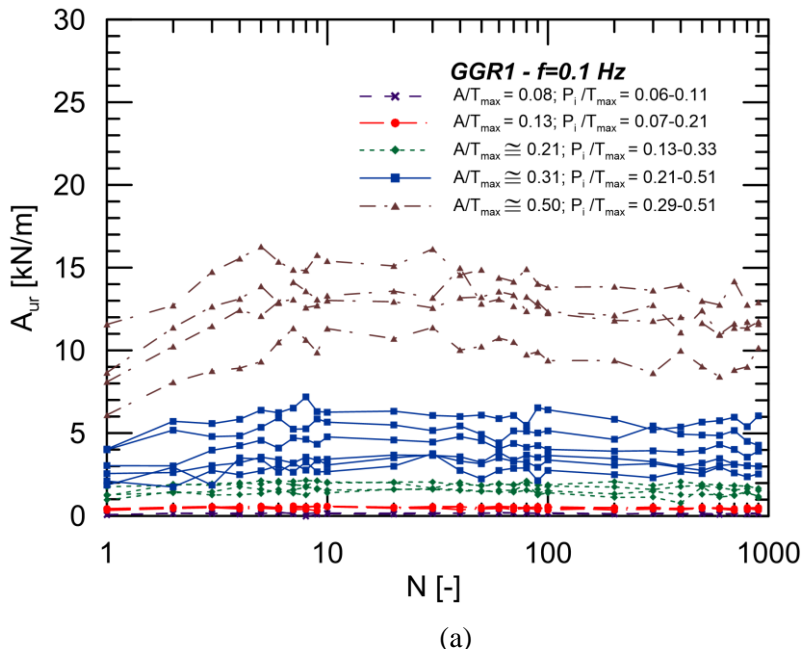
515 *Figure 3. Unload and reload stiffness for varying number of loading cycles, for test with $P_i/T_{max}=0.33$*

516 *and $A/T_{max}=0.52$ (a); and hysteretic stiffness for tests with $P_i/T_{max}=0.33$ and different A/T_{max} (b) at*

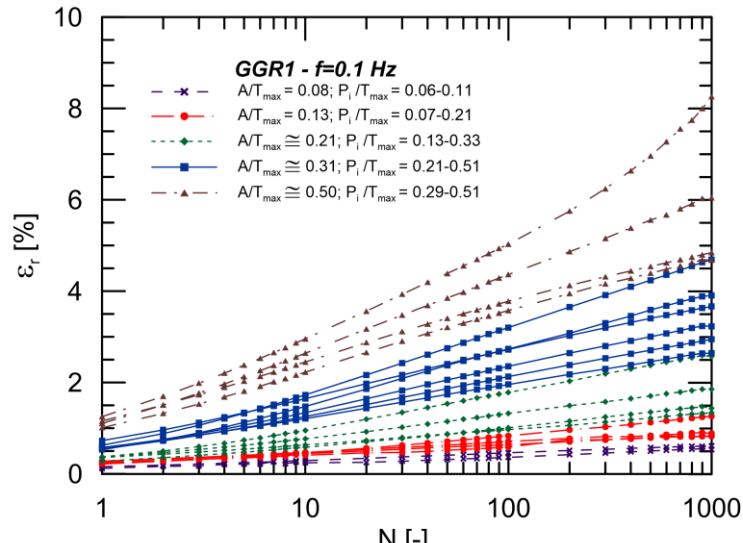
517 *different frequencies.*



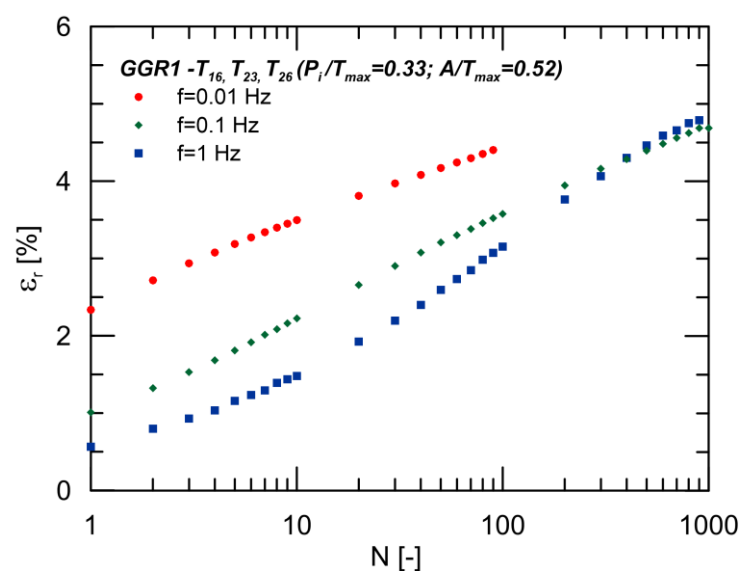
520 *Figure 4. Unload stiffness for number of loading cycles $N=1$ (a); $N=10$ (b); and $N=1000$ (c); and reload*
 521 *stiffness for number of loading cycles $N=1$ (d); $N=10$ (e); and $N=1000$ (f), versus normalised loading*
 522 *amplitudes, for different ranges of normalised pre-stress loads and $f=0.1$ Hz.*



526 *Figure 5. Hysteretic area for varying number of loading cycles, for all tests performed at $f=0.1$ Hz (a)*
 527 *and for tests with $P_i/T_{\max}=0.33$ and $A/T_{\max}=0.52$ at different frequencies (b).*

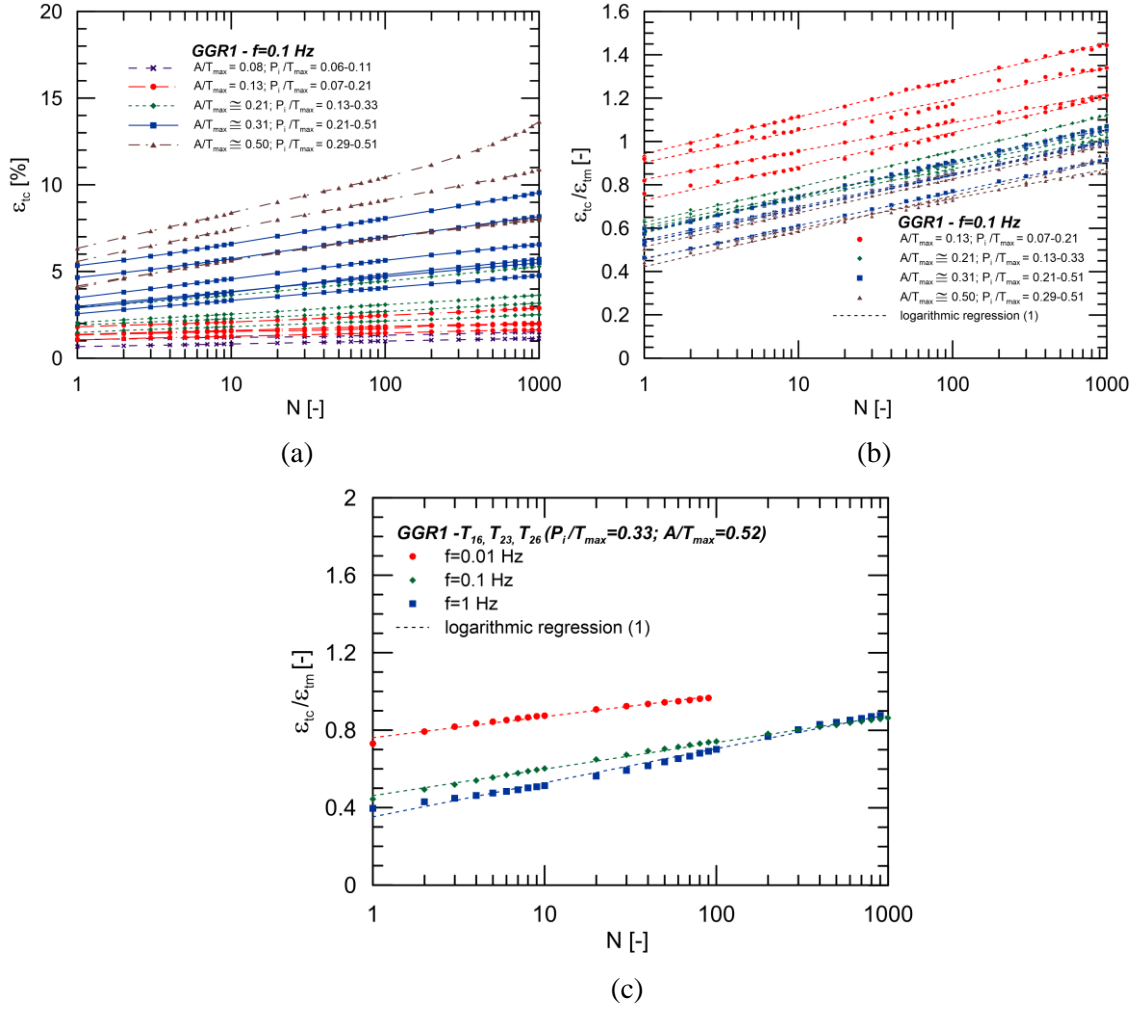


(a)

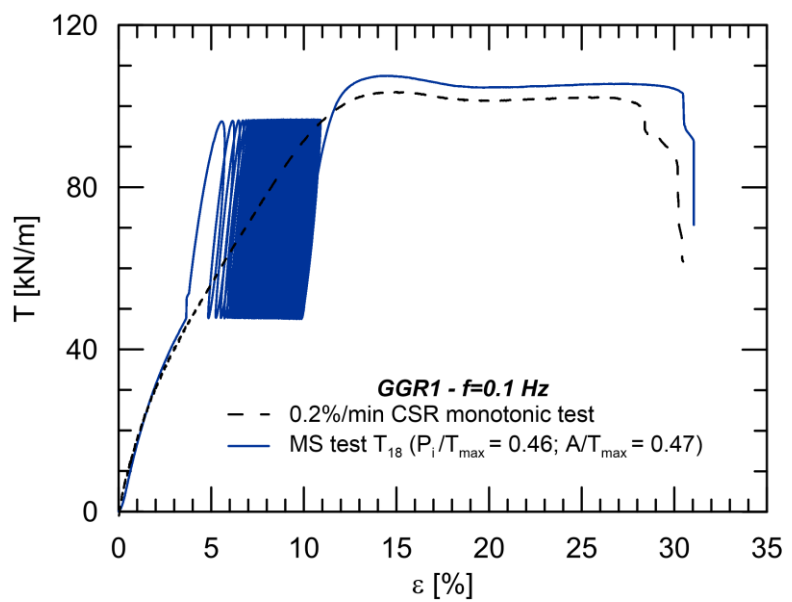


(b)

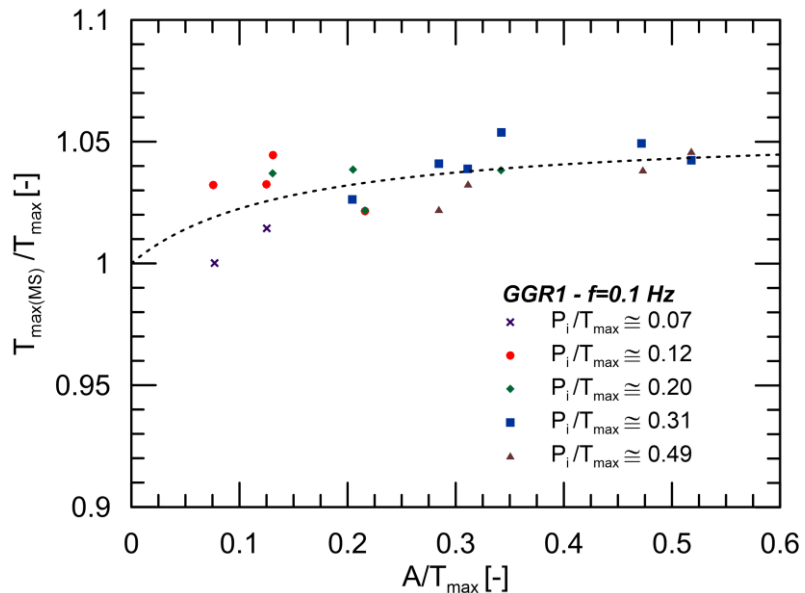
531 *Figure 6. Residual strain trends for varying number of loading cycles, for all tests performed at $f=0.1$*
 532 *Hz (a) and for tests with $P_i/T_{max}=0.33$ and $A/T_{max}=0.52$ at different frequencies (b).*



536 *Figure 7. Maximum strain trends (a) and $\varepsilon_{tc}/\varepsilon_{tm}$ ratios (b) for varying number of loading cycles and*
 537 *for all tests performed at $f=0.1$ Hz; and $\varepsilon_{tc}/\varepsilon_{tm}$ ratios for tests with $P_i/T_{max}=0.33$ and $A/T_{max}=0.52$ at*
 538 *different frequencies (c).*

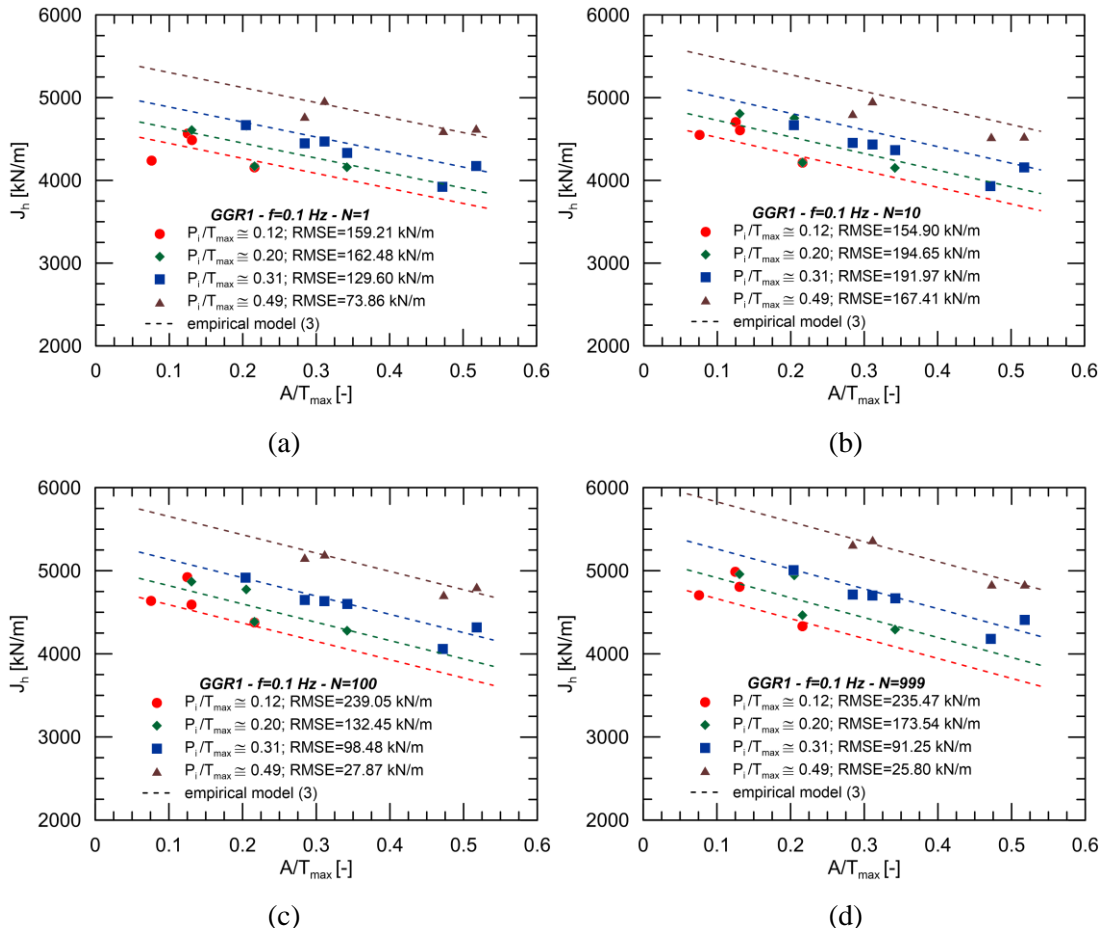


(a)



(b)

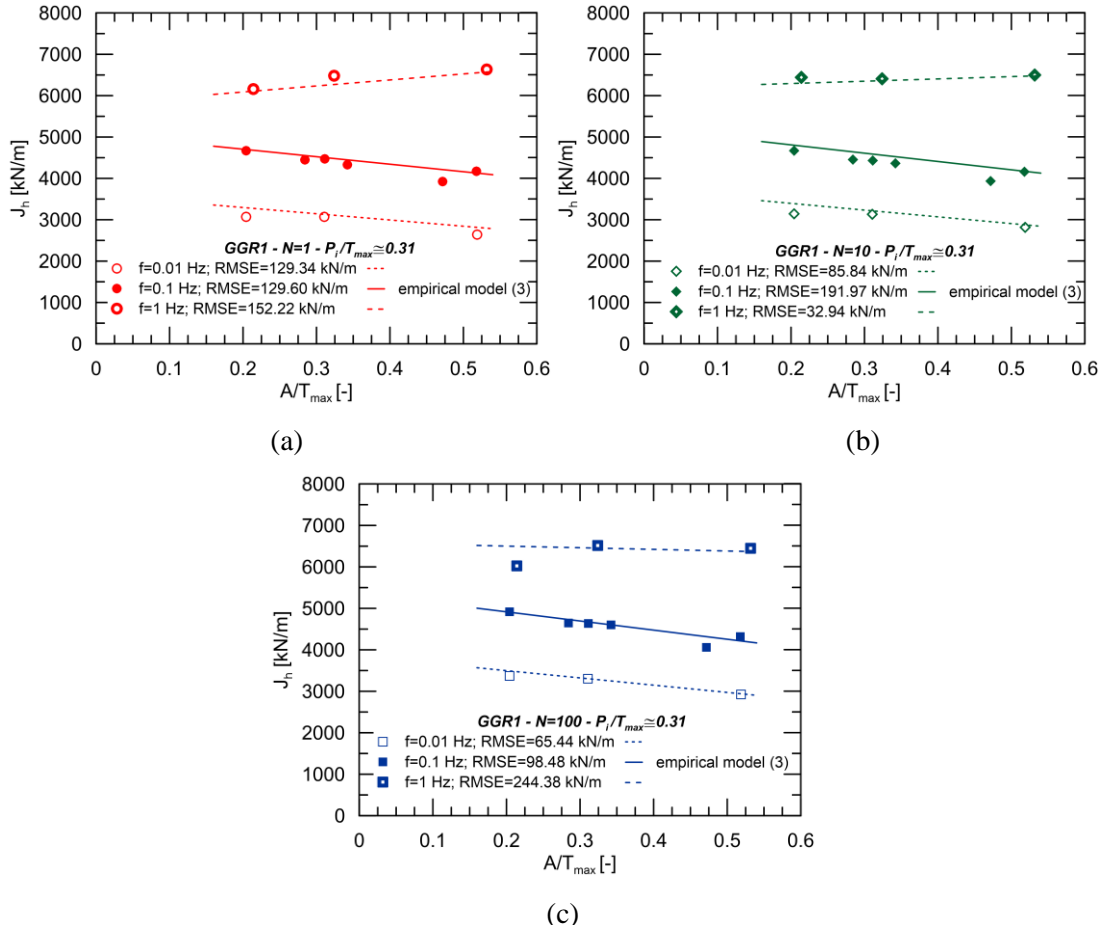
542 *Figure 8. Typical load-strain trends obtained in monotonic and multistage conditions (a) and*
 543 *normalised maximum tensile strength for varying normalised loading amplitudes and for different*
 544 *ranges of normalised pre-stress loads (b) at $f=0.1$ Hz.*



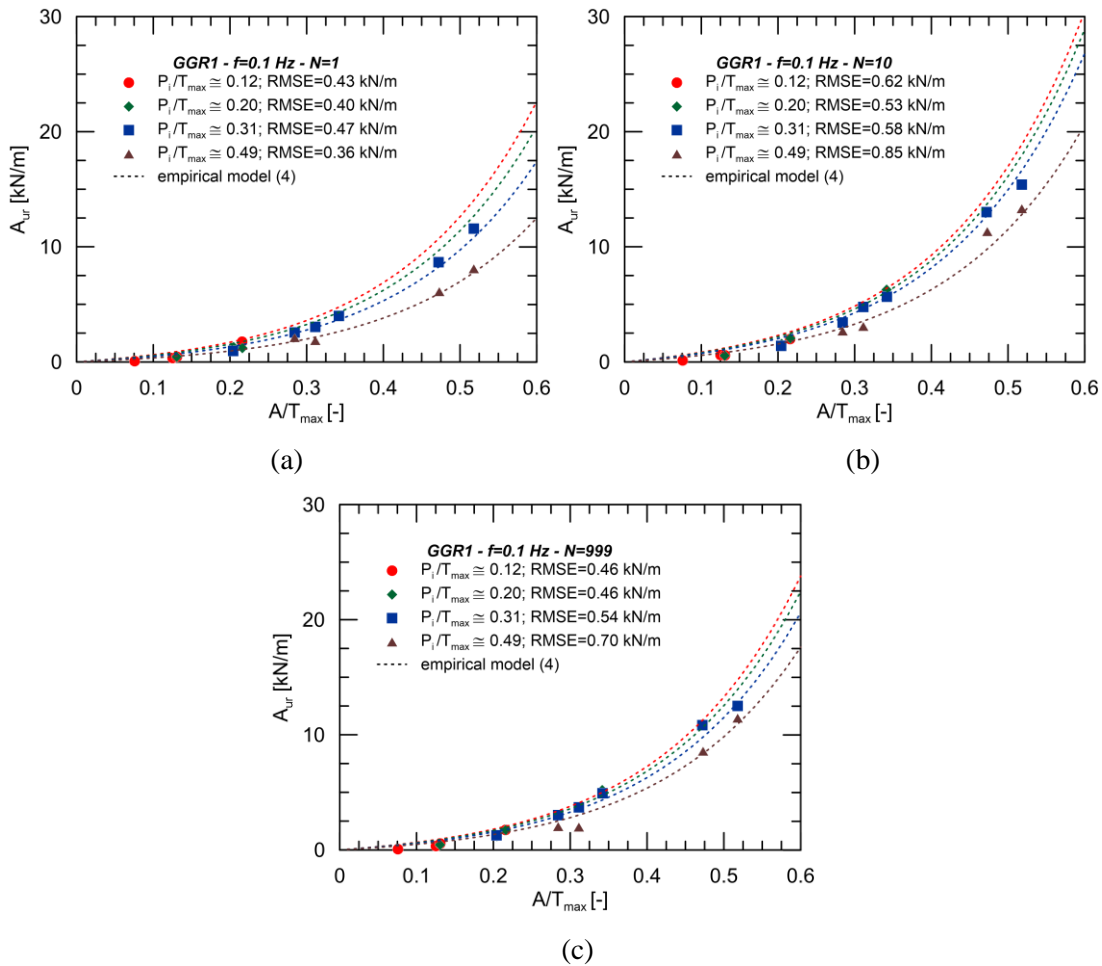
546

547 *Figure 9. Predicted and experimental values of GGR1 hysteretic stiffness for varying normalised
 548 loading amplitudes, for different ranges of normalised pre-stress loads and $f=0.1$ Hz at numbers of
 549 loading cycles $N=1$ (a); $N=10$ (b); $N=100$ (c); and $N=999$ (d).*

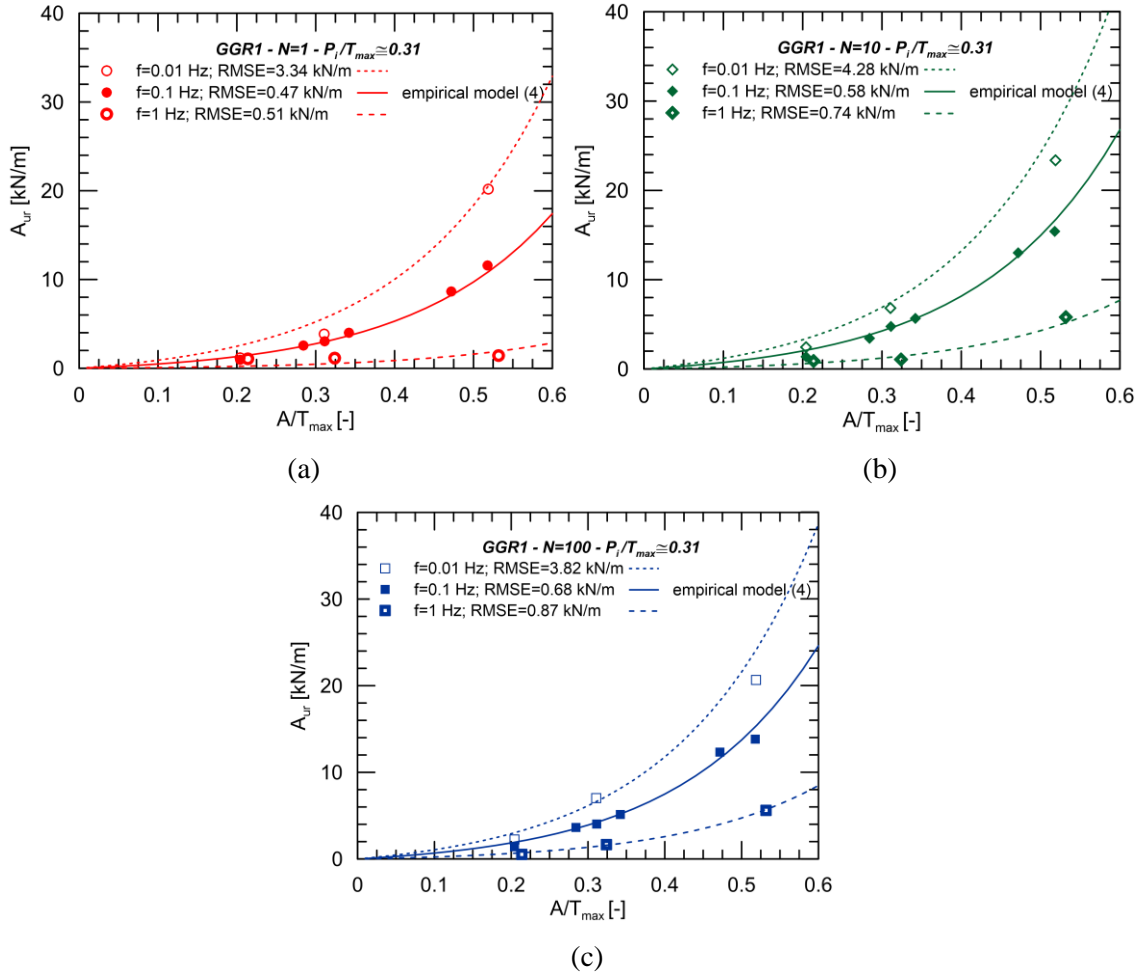
550



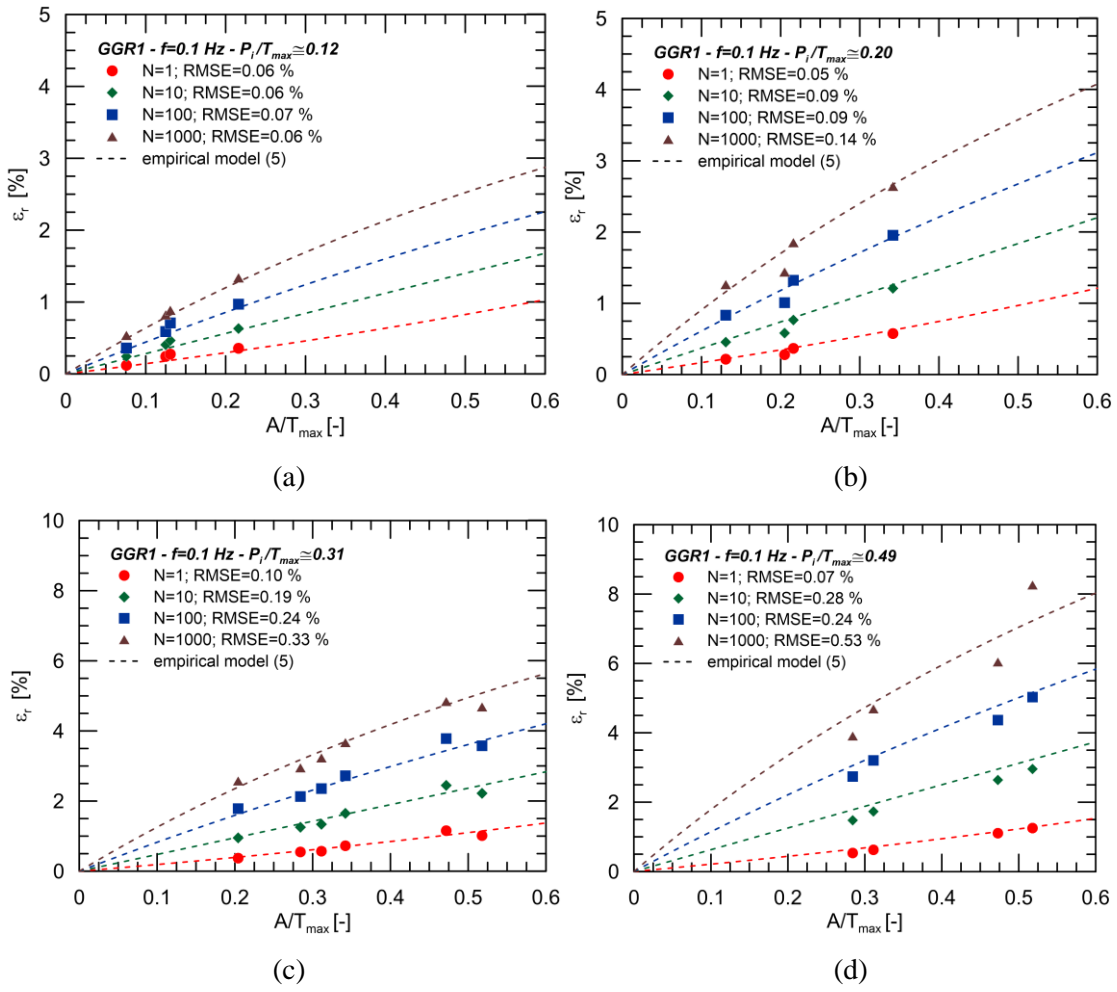
553 *Figure 10. Predicted and experimental values of GGR1 hysteretic stiffness for varying normalised
554 loading amplitudes, for a fixed normalised pre-stress load class and different frequencies, at numbers
555 of loading cycles $N=1$ (a); $N=10$ (b); and $N=100$ (c).*



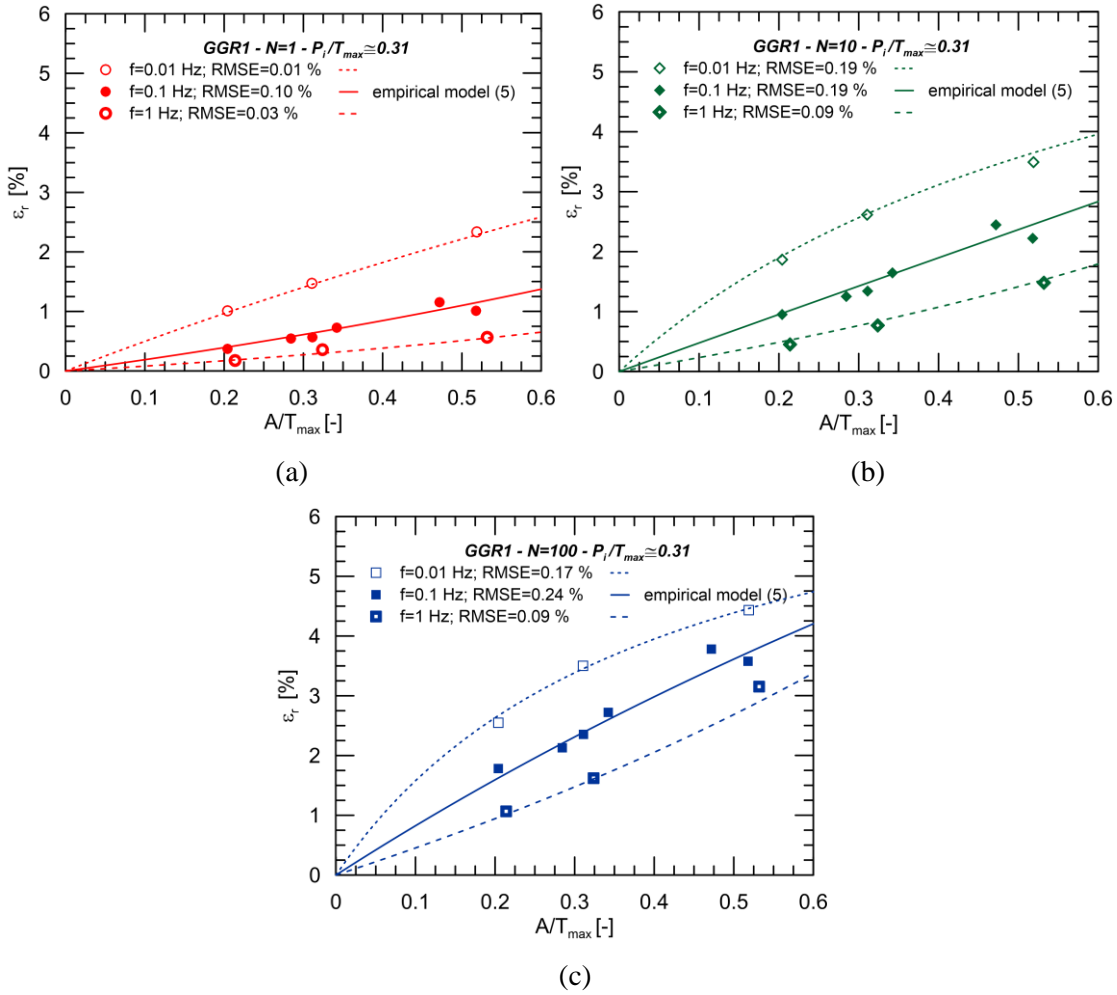
559 *Figure 11. Predicted and experimental values of GGR1 hysteretic area for varying normalised loading*
 560 *amplitudes, for different ranges of normalised pre-stress loads and $f=0.1 \text{ Hz}$, at numbers of loading*
 561 *cycles $N=1$ (a); $N=10$ (b); and $N=999$ (c).*



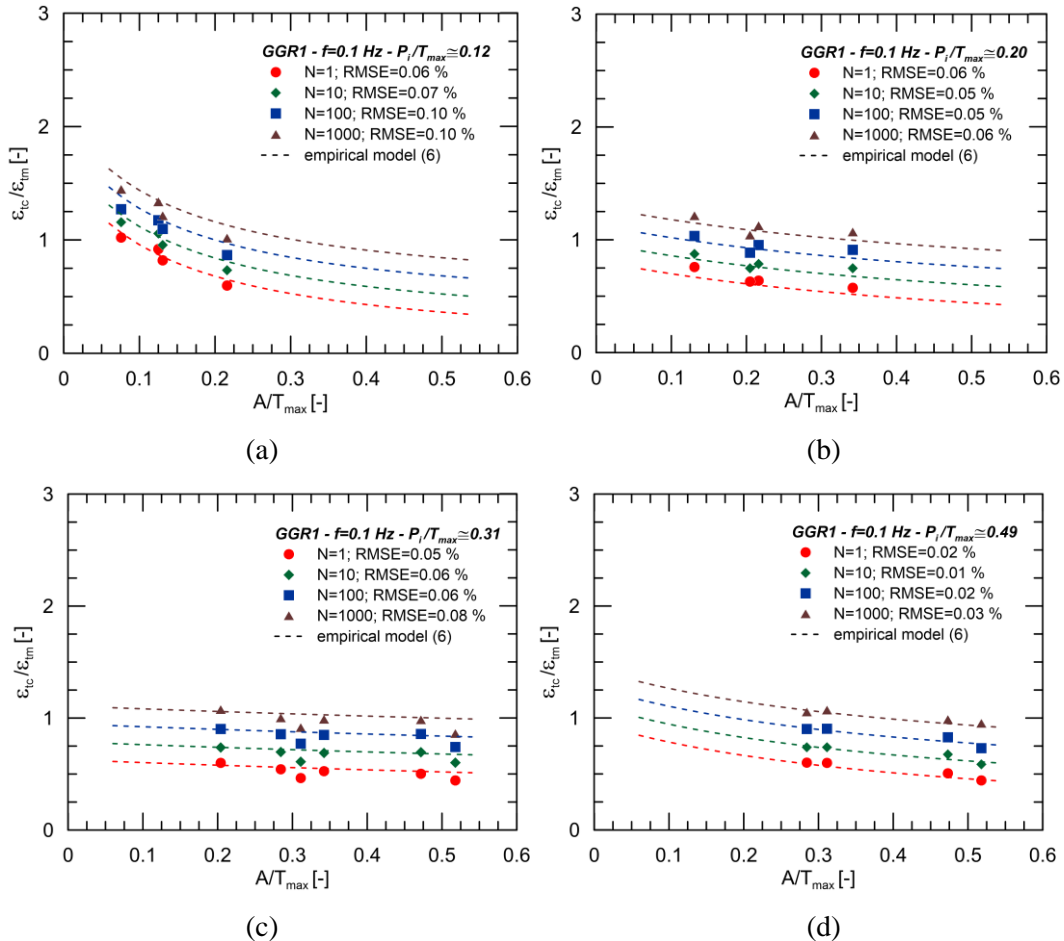
565 *Figure 12. Predicted and experimental values of GGR1 hysteretic area for varying normalised loading*
 566 *amplitudes, for a fixed normalised pre-stress load class and at different frequencies, at numbers of*
 567 *loading cycles $N=1$ (a); $N=10$ (b); and $N=100$ (c).*



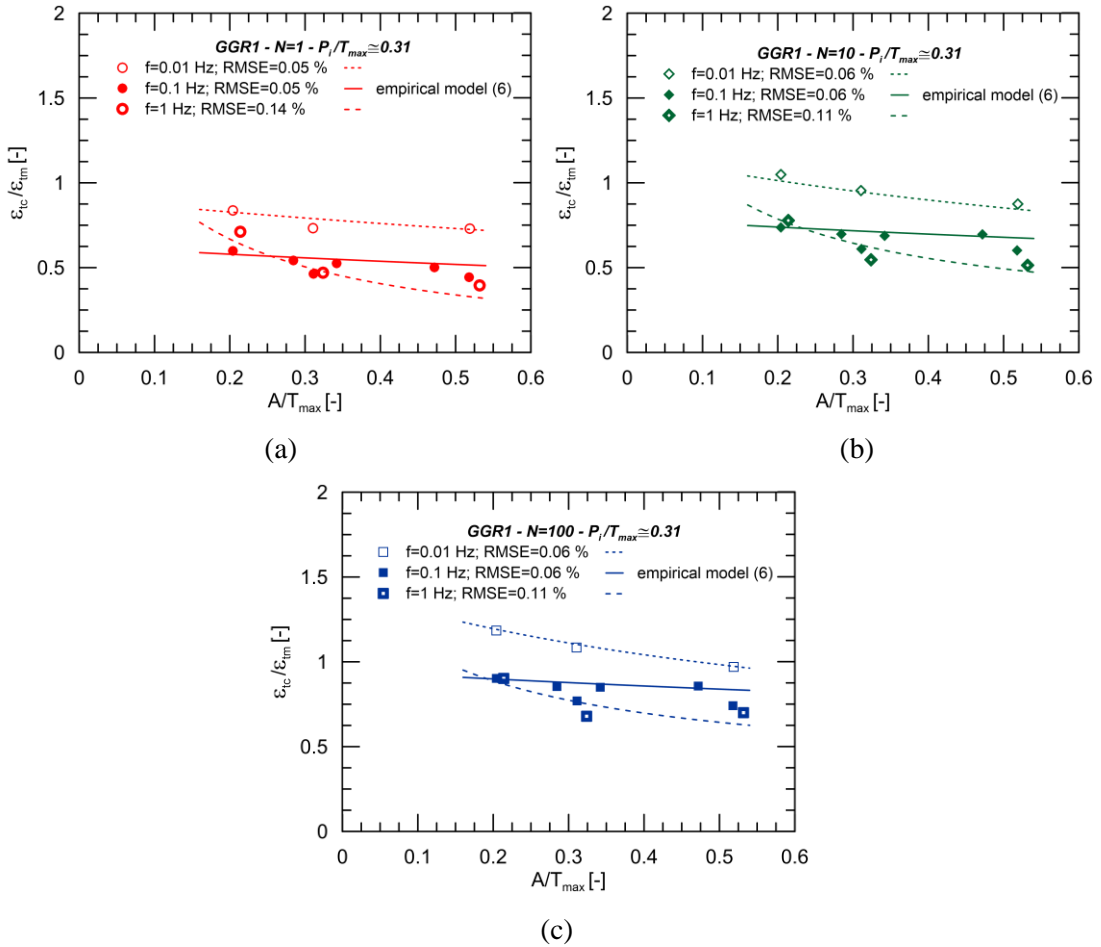
571 *Figure 13. Predicted and experimental values of GGR1 residual strain for varying normalised loading*
 572 *amplitudes, for different loading cycles and $f=0.1$ Hz, at normalised pre-stress load classes*
 573 $P_i/T_{max} \approx 0.12$ (a); $P_i/T_{max} \approx 0.20$ (b); $P_i/T_{max} \approx 0.31$ (c); and $P_i/T_{max} \approx 0.49$ (d).



577 *Figure 14. Predicted and experimental values for GGR1 residual strain for varying normalised*
 578 *loading amplitudes, for a fixed normalised pre-stress load class and at different frequencies, at*
 579 *numbers of loading cycles $N=1$ (a); $N=10$ (b); and $N=100$ (c).*



583 *Figure 15. Predicted and experimental values of the $\varepsilon_{tc}/\varepsilon_{tm}$ ratio for varying normalised loading*
 584 *amplitudes, for different numbers of loading cycles and $f=0.1$ Hz, at normalised pre-stress load*
 585 *classes $P_i/T_{max} \approx 0.12$ (a); $P_i/T_{max} \approx 0.20$ (b); $P_i/T_{max} \approx 0.31$ (c); and $P_i/T_{max} \approx 0.49$ (d).*



589 *Figure 16. Predicted and experimental values for the $\varepsilon_{tc}/\varepsilon_{tm}$ ratio for varying normalised loading
590 amplitudes, for a fixed normalised pre-stress load class and at different frequencies, at numbers of
591 loading cycles N=1 (a); N=10 (b); and N=100 (c).*

594 **ACKNOWLEDGEMENTS**

595 All authors contributed equally to this work. They would like to acknowledge the assistance of Ing. P.

596 Recalcati.

597

599 **7 REFERENCES**

- 600 Ashmawy, A.K. & Bourdeau, P.L. (1996) Response of a woven and a nonwoven geotextile to
601 monotonic and cyclic simple tension Geosynthetics International, 3(4): 493–515
- 602 ASTM (2010) D 7556: Standard test method for determining small-strain tensile properties of
603 geogrids and geotextiles by in-air cyclic tension tests. American Society for Testing and Materials,
604 West Conshohocken, Pennsylvania, USA
- 605 ASTM (2011) D 4595: Standard test method for tensile properties of geotextiles by the wide-width
606 strip method. American Society for Testing and Materials, West Conshohocken, Pennsylvania, USA
- 607 Bathurst, R.J., Allen, T.M., Walters, D.L. (2002) Short-term strain and deformation behavior of
608 geosynthetic walls at working stress conditions. Geosynthetics International, 9(5-6): 451-482
- 609 Bathurst, R.J. & Cai, Z. (1994) In-Isolation cyclic load-extension behavior of two geogrids.
610 Geosynthetics International, 1(1): 1-19
- 611 Bathurst, R.J. & Ezzein, F.M. (2015) Geogrid pullout load–strain behaviour and modelling using a
612 transparent granular soil. Geosynthetics International. [<http://dx.doi.org/10.1680/jgein.15.00051>]
- 613 Calvarano, L.S., Gioffrè, D., Cardile, G., Moraci, N. (2014) A stress transfer model to predict the
614 pullout resistance of extruded geogrids embedded in compacted granular soils. In proceeding of the
615 10th International Conference on Geosynthetics, ICG 2014. Berlin, Germany, 21-24 September 2014,
616 Code 110984.
- 617 Cardile, G., Calvarano, L.S., Gioffrè, D., Moraci, N. (2014) Experimental evaluation of the pullout
618 active length of different geogrids. In proceeding of the 10th International Conference on
619 Geosynthetics, ICG 2014. Berlin, Germany, 21-25 September 2014, Code 110984.
- 620 Cardile, G., Moraci, N., Calvarano, L.S. (2016) Geogrid pullout behaviour according to the
621 experimental evaluation of the active length. Geosynthetics International, 23(3):194-205,
622 [<http://dx.doi.org/10.1680/jgein.15.00042>]
- 623 Cazzuffi, D., Calvarano, L.S., Cardile, G., Moraci, N., Recalcati, P. (2011) European experience in
624 pullout tests: The influence of geogrid's geometry and structure on interface behaviour. Geosynthetics,
625 29(5): 42- 51
- 626 Cazzuffi, D., Moraci, N., Calvarano, L.S., Cardile, G., Gioffrè, D., Recalcati, P. (2014) The influence
627 of vertical effective stress and of geogrid length on interface behaviour under pullout conditions.
628 Geosynthetics, 32(2): 40-50

- 629 Dixon, N. (2010) Soil-geosynthetic interaction: interface behaviour. In proceeding of the Proceedings,
630 9th International Conference on Geosynthetics. International Geosynthetics Society Guaruja, Brazil,
631 May 23rd-27th, 563-582
- 632 Drozdov, A.D. & Christiansen, J.d. (2007) Viscoelasticity and viscoplasticity of semicrystalline
633 polymers: Structure–property relations for high-density polyethylene. Computational Materials
634 Science, 39: 729-751
- 635 Ezzein, F.M. & Bathurst, R.J. (2014) A new approach to evaluate soil-geosynthetic interaction using a
636 novel pullout test apparatus and transparent granular soil. Geotextiles and Geomembranes, 42(3): 246-
637 255
- 638 Ezzein, F.M., Bathurst, R.J., Kongkitkul, W. (2015) Nonlinear load–strain modeling of polypropylene
639 geogrids during constant rate-of-strain loading. Polymer Engineering and Science, 55(7): 1617–1627
- 640 Hirakawa, D., Kongkitkul, W., Tatsuoka, F., Uchimura, T. (2003) Time-dependent stress–strain
641 behaviour due to viscous properties of geogrid reinforcement. Geosynthetics International, 10(6):
642 176-199
- 643 Hussein, M.G. & Meguid, M.A. (2016) A three-dimensional finite element approach for modeling
644 biaxial geogrid with application to geogrid-reinforced soils. Geotextiles and Geomembranes, 44(3):
645 295-307
- 646 ISO (1976) 554: Standard atmospheres for conditioning and/or testing—Specifications. International
647 Organization for Standardization, Geneva, Switzerland
- 648 ISO (2015) 10319: Geosynthetics Wide-width Tensile Test. International Organization for
649 Standardization, Geneva, Switzerland
- 650 Kongkitkul, W., Hirakawa, D., Tatsuoka, F., Uchimura, T. (2004) Viscous deformation of
651 geosynthetic reinforcement under cyclic loading conditions and its model simulation. Geosynthetics
652 International, 11(2): 73-99
- 653 Koseki, J., Tatsuoka, F., Watanabe, K., Tateyama, M., Kojima, K. and Munaf, Y. (2003) Model tests
654 on seismic stability of several types of soil retaining walls, Reinforced Soil Engineering, Ling,
655 Leshchinsky and Tatsuoka (eds.), Dekker, 317-358
- 656 Koseki, J., Bathurst, R.J., Guler, E., Kuwano, J., Maugeri, M. (2006) Seismic stability of reinforced
657 soil walls. In proceeding of the 8th International Conference on Geosynthetics. Yokohama, Japan, 18-
658 22 September, 28 p.
- 659 Kuwano, J., Miyata, Y., Koseki, J. (2014) Performance of reinforced soil walls during the 2011
660 Tohoku earthquake. Geosynthetics International, 21(3): 179–196

- 661 Lee, K.Z.Z. & Wu, J.T.H. (2004) A synthesis of case histories on GRS bridge supporting structures
662 with flexible facing. *Geotextiles and Geomembranes*, 22: 181-204
- 663 Ling, H.I., Leshchinsky, D., Chou, N.N.S. (2001) Post-earthquake investigation on several
664 geosynthetic-reinforced soil retaining walls and slopes during the Ji-Ji earthquake of Taiwan. *Soil*
665 dynamics and earthquake engineering, 21: 297-313
- 666 Ling, H.I., Mohri, Y., Kawabata, T. (1998) Tensile properties of geogrids under cyclic loadings.
667 *Journal of Geotechnical and Geoenvironmental Engineering*, 124(8): 782-787
- 668 Liu, C.-N., Zornberg, J.G., Chen, T.-C., Ho, Y.-H., Lin, B.-H. (2009) Behavior of geogrid-sand
669 interface in direct shear mode. *Journal of Geotechnical and Geoenvironmental Engineering*, 135(12):
670 1863-1871
- 671 Liu, F.-Y., Wang, P., Geng, X., Wang, J., Lin, X. (2016) Cyclic and post-cyclic behaviour from sand–
672 geogrid interface large-scale direct shear tests. *Geosynthetics International*, 23(2): 129-139
- 673 Liu, H. & Ling, H.I. (2005) Constitutive modeling of the time-dependent monotonic and cyclic
674 behavior of geosynthetics. In proceeding of the Geosynthetics and Geosynthetic-Engineered Soil
675 Structures (McMat 2005 Conference). Baton Rouge, Louisiana, USA.
- 676 Liu, H. & Ling, H.I. (2007) Unified elastoplastic-viscoplastic bounding surface model of
677 geosynthetics and its applications to Geosynthetic Reinforced Soil-Retaining Wall Analysis. *Journal of*
678 *Engineering Mechanics*, 133(7): 801-815
- 679 Mendonca, A. & Lopes, M.d.L. (2011) Role of the damping ratio of reinforcement on the behaviour of
680 geogrids-reinforced systems. *Geotechnical and Geological Engineering*, 29: 375-388
- 681 Moraci, N. & Cardile, G. (2008) Pull-out behaviour of different geosynthetics embedded in granular
682 soils. In proceeding of the 4th Asian Regional Conference on Geosynthetics. Shanghai, China, 17-20
683 June, 146-150
- 684 Moraci, N. & Cardile, G. (2009) Influence of cyclic tensile loading on pullout resistance of geogrids
685 embedded in a compacted granular soil. *Geotextiles and Geomembranes*, 27(6): 475-487.
686 [10.1016/j.geotexmem.2009.09.019]
- 687 Moraci, N. & Cardile, G. (2012) Deformative behaviour of different geogrids embedded in a granular
688 soil under monotonic and cyclic pullout loads. *Geotextiles and Geomembranes*, 32(1): 104-110.
689 [10.1016/j.geotexmem.2011.11.001]
- 690 Moraci, N., Cazzuffi, D., Calvarano, L.S., Cardile, G., Gioffrè, D., Recalcati, P. (2014) The influence
691 of soil type on interface behavior under pullout conditions. *Geosynthetics*, 32(3): 42-50
- 692 Moraci, N. & Montanelli, F. (1997) Behavior of geogrids under cyclic loads. In proceeding of the
693 Geosynthetics '97. Long Beach, CA, USA, March, 961-976

- 694 Moraci, N. & Recalcati, P. (2006) Factors affecting the pullout behaviour of extruded geogrids
695 embedded in compacted granular soil. *Geotextiles and Geomembranes*, 24(4): 220-242
- 696 Palmeira, E.M. (2009) Soil–geosynthetic interaction: Modelling and analysis. *Geotextiles and*
697 *Geomembranes*, 27(5): 368-390
- 698 Perkins, S.W. (2000) Constitutive modeling of geosynthetics. *Geotextiles and Geomembranes*, 18(5):
699 273-292
- 700 Sieira, A.C.C.F., Gerscovich, D.M.S., Sayao, A.S.F.J. (2009) Displacement and load transfer
701 mechanisms of geogrids under pullout condition. *Geotextiles and Geomembranes*, 27(4): 241-253
- 702 Tatsuoka, F., Koseki, J., Tateyama, M. (1995) Performance of geogrid-reinforced soil retaining walls
703 during the Great Hanshin-Awaji Earthquake. In proceeding of the 1st International Conference on
704 Earthquake Geotechnical Engineering, Tokyo, Japan, January 17, 55-62
- 705 Vieira, C.S. & Lopes, M.d.L. (2013) Effects of the loading rate and cyclic loading on the strength and
706 deformation properties of a geosynthetic. *Construction and Building Materials*, 49: 758-765
- 707 Zanzinger, H., Hangen, H., Alexiew, D. (2010) Fatigue behaviour of a PET-Geogrid under cyclic
708 loading. *Geotextiles and Geomembranes*, 28(3): 251-261
- 709 Zhou, J., Chen, J.-F., Xue, J.-F., Wang, J.-Q. (2012) Micro-mechanism of the interaction between sand
710 and geogrid transverse ribs. *Geosynthetics International*, 19(6): 426-437
- 711
- 712

714 **Figure captions**

715 Figure 1. Scheme of the equipment used for tensile testing the geogrid specimen (a); in detail:	
716 hydraulic clamps (b); hydrostatic bearing actuator (c); hydraulic unit (d).....	24
717 Figure 2. Multistage procedure (a) and schematic representation of different parameters obtained	
718 during hysteresis loops in multistage tests (b).....	25
719 Figure 3. Unload and reload stiffness for varying number of loading cycles, for test with $P_i/T_{max}=0.33$	
720 and $A/T_{max}=0.52$ (a); and hysteretic stiffness for tests with $P_i/T_{max}=0.33$ and different A/T_{max} (b) at	
721 different frequencies.....	26
722 Figure 4. Unload stiffness for number of loading cycles $N=1$ (a); $N=10$ (b); $N=1000$ (c); and reload	
723 stiffness for number of loading cycles $N=1$ (d); $N=10$ (e); and $N=1000$ (f), versus normalised loading	
724 amplitudes, for different ranges of normalised pre-stress loads and $f=0.1$ Hz.....	27
725 Figure 5. Hysteretic area for varying number of loading cycles, for all tests performed at $f=0.1$ Hz (a)	
726 and for tests with $P_i/T_{max}=0.33$ and $A/T_{max}=0.52$ at different frequencies (b).....	28
727 Figure 6. Residual strain trends for varying number of loading cycles, for all tests performed at $f=0.1$	
728 Hz (a) and for tests with $P_i/T_{max}=0.33$ and $A/T_{max}=0.52$ at different frequencies (b).....	29
729 Figure 7. Maximum strain trends (a) and $\varepsilon_{tc}/\varepsilon_{tm}$ ratios (b) for varying number of loading cycles and for	
730 all tests performed at $f=0.1$ Hz; and $\varepsilon_{tc}/\varepsilon_{tm}$ ratios for tests with $P_i/T_{max}=0.33$ and $A/T_{max}=0.52$ at	
731 different frequencies (c). ..	30
732 Figure 8. Typical load-strain trends obtained in monotonic and multistage conditions (a) and	
733 normalised maximum tensile strength for varying normalised loading amplitudes and for different	
734 ranges of normalised pre-stress loads (b) at $f=0.1$ Hz.	31
735 Figure 9. Predicted and experimental values of GGR1 hysteretic stiffness for varying normalised	
736 loading amplitudes, for different ranges of normalised pre-stress loads and $f=0.1$ Hz at numbers of	
737 loading cycles $N=1$ (a); $N=10$ (b); $N=100$ (c); and $N=999$ (d).	32
738 Figure 10. Predicted and experimental values of GGR1 hysteretic stiffness for varying normalised	
739 loading amplitudes, for a fixed normalised pre-stress load class and different frequencies, at numbers	
740 of loading cycles $N=1$ (a); $N=10$ (b); and $N=100$ (c).....	33
741 Figure 11. Predicted and experimental values of GGR1 hysteretic area for varying normalised loading	
742 amplitudes, for different ranges of normalised pre-stress loads and $f=0.1$ Hz, at numbers of loading	
743 cycles $N=1$ (a); $N=10$ (b); and $N=999$ (c). ..	34

744	Figure 12. Predicted and experimental values of GGR1 hysteretic area for varying normalised loading amplitudes, for a fixed normalised pre-stress load class and at different frequencies, at numbers of loading cycles N=1 (a); N=10 (b); and N=100 (c).....	35
747	Figure 13. Predicted and experimental values of GGR1 residual strain for varying normalised loading amplitudes, for different loading cycles and f=0.1 Hz, at normalised pre-stress load classes P _i /T _{max} ≈0.12 (a); P _i /T _{max} ≈0.20 (b); P _i /T _{max} ≈0.31 (c); and P _i /T _{max} ≈0.49 (d).....	36
750	Figure 14. Predicted and experimental values for GGR1 residual strain for varying normalised loading amplitudes, for a fixed normalised pre-stress load class and at different frequencies, at numbers of loading cycles N=1 (a); N=10 (b); and N=100 (c).....	37
753	Figure 15. Predicted and experimental values of the $\varepsilon_{tc}/\varepsilon_{tm}$ ratio for varying normalised loading amplitudes, for different numbers of loading cycles and f=0.1 Hz, at normalised pre-stress load classes P _i /T _{max} ≈0.12 (a); P _i /T _{max} ≈0.20 (b); P _i /T _{max} ≈0.31 (c); and P _i /T _{max} ≈0.49 (d).....	38
756	Figure 16. Predicted and experimental values for the $\varepsilon_{tc}/\varepsilon_{tm}$ ratio for varying normalised loading amplitudes, for a fixed normalised pre-stress load class and at different frequencies, at numbers of loading cycles N=1 (a); N=10 (b); and N=100 (c).....	39
759		